

ABSTRACT

Title of thesis: GUIDED LAMB WAVE
 STRUCTURAL HEALTH
 MONITORING TECHNIQUES FOR
 AIRCRAFT APPLICATIONS

Jacob Ryan McCullum
Master of Science, 2019

Thesis directed by: Professor Norman M. Wereley
 Department of Aerospace Engineering

Growing aerospace industry interest in structural health monitoring (SHM) has led to the development of many damage detection and localization techniques which make use of guided Lamb Waves (GLW). To continue this growth, further development of these techniques is necessary with an industry-focused mindset through studies with realistic, complex aircraft structures. The present study applies GLW techniques to two aircraft structures and examines the feasibility of their use for practical SHM applications. Particularly this work focuses on evaluating the effects of complex structural features found in aircraft, examining the human interaction with GLW techniques, and enhancing GLW techniques using nontraditional dual PZT transducers. Several damage case studies are performed showing that damage can be detected and located, and limitations to the techniques are characterized. Moreover, the use of dual PZT transducers shows improvements to damage localization techniques which potentially enable greater flexibility for aircraft applications.

GUIDED LAMB WAVE STRUCTURAL HEALTH MONITORING
TECHNIQUES FOR AIRCRAFT APPLICATIONS

by

Jacob Ryan McCullum

Thesis submitted to the Faculty of the Graduate School of the
University of Maryland, College Park in partial fulfillment
of the requirements for the degree of
Master of Science
2019

Advisory Committee:
Professor Norman M. Wereley, Chair/Advisor
Professor Darryll J. Pines
Professor Sung W. Lee
Dr. Byungseok Yoo

© Copyright by
Jacob Ryan McCullum
2019

Acknowledgments

First, I can't ever be thankful enough that I met my God and my Savior, Jesus Christ during the end of my time here at UMD. His love has truly transformed my life and given me the strength I needed to finish my graduate studies.

Thank you to Dr. Wereley for giving me an opportunity to do research at the end of my Sophomore year. I will always be thankful for his guidance, help with networking, and motivation to pursue a graduate degree. I am also deeply thankful for Dr. Yoo who taught me a great amount about Lamb Waves. I am incredibly grateful for his encouragement, ideas, and patience as I learned from him. I could not have accomplished what I did without him. Thank you also to Dr. Pines and Dr. Lee for taking the time to serve on my committee.

I was fortunate to have great friends to work with in the CORE lab. Jacek, Jon, Rebecca, and Tom, I am thankful for our banter, support for each other's hardships, friendly debates, and fun times together. I am especially grateful for Chinonso who's fellowship and guidance has helped me grow exponentially in my faith at this turning point in my life.

Thank you to the SMART Scholarship program for funding my graduate education and providing me with a secure start to my career. I can't recommend this program enough. Thank you to Steve Donaldson and Bob David for helping me get my foot in the door at NAVAIR, and thank you to my Pax River colleagues for their mentorship and encouragement. I am so excited to begin working full time with you all.

Finally, thank you to my family and especially you, Mom and Dad for your unconditional love and support. Simply put, I would be nowhere without you.

Table of Contents

Acknowledgements	ii
Table of Contents	iv
List of Tables	vi
List of Figures	vii
List of Abbreviations	ix
1 Introduction	1
1.1 Motivation	1
1.2 Structural Health Monitoring	2
1.3 Guided Lamb Waves	4
1.4 Scope of Thesis	9
2 F/A-18 Wing Torque Loss Monitoring	11
2.1 Introduction	11
2.2 Guided Lamb Wave Damage Localization Techniques	13
2.2.1 Total Focusing Method (TFM)	13
2.2.2 Sign Coherence Factor (SCF) Imaging	15
2.2.3 Experimental Setup	17
2.3 Damage Detection Image Results	21
2.3.1 Single Bolt Torque Loss Images	22
2.3.2 Single Group Torque Loss Images	23
2.3.3 Multiple Group Torque Loss Images	26
2.4 Autonomous Damage Detection	27
2.4.1 Image Cross-Correlation	27
2.4.2 Group Velocity Correction and Filtering	30
2.4.3 Damage Image Maxima Method	34
2.4.4 Discussion	35
2.5 Manual Technician Review Study	36
2.6 Chapter Conclusion	41
3 Piper Cherokee Wing Damage Localization	43
3.1 Introduction	43
3.2 Methodology	45

3.2.1	Dual PZTs and Mode Decomposition	45
3.2.1.1	Empirical Scaling Factor Determination	47
3.2.2	Sparse Array Technique	51
3.2.3	Experimental Setup	53
3.2.3.1	Piper Cherokee Wing	53
3.2.3.2	Magnet Damage Simulation	54
3.2.3.3	Data Acquisition	55
3.3	Results and Discussion	57
3.3.1	Magnet Damage Simulation Validation	58
3.3.2	Wing Case Study 1 - Basic Damage Assessment	59
3.3.3	Wing Case Study 2 - Damage Far from the Array	62
3.3.4	Wing Case Study 3 - Damage within the Array	62
3.3.5	Wing Case Study 4 - Damage Across the Leading Edge	64
3.3.6	Wing Case Study 5 - Damage Across a Lap Joint	65
3.4	Chapter Conclusion	71
4	Conclusion	73
4.1	F/A-18 Wing Torque Loss Monitoring	73
4.2	Piper Cherokee Wing Damage Localization	75
4.3	Future Work	76
A	Blind Technician Study Details	78
A.1	Contents of Study Presented to Participants	78
A.1.1	Instructions	78
A.1.2	Procedure	79
	Bibliography	89

List of Tables

1.1	SHM Classification Levels	4
2.1	Blind study results for the seven individual cases and the sum of all cases	39
3.1	Ratios of S0 amplitudes between RD_{ij} and DD_{ij} , $S_{c,ij}$	49
3.2	Ratios of A0 amplitudes between RD_{ij} and DD_{ij} , $A_{c,ij}$	49

List of Figures

1.1	Aviation fatigue examples and incidents.	3
1.2	Dispersion curves for Al2024-T3 with thickness 1 mm.	6
1.3	A0 and S0 modes 600 mm from a 100 kHz 4.5 cycle excitation in Al2024-T3 with thickness 1 mm.	6
1.4	Tuning curves for 1mm thick Al2024-T3 and 6.3 mm dia. PZT	7
1.5	GLW pitch-catch propagation in a plate.	8
1.6	Ideal single mode, nondispersive pitch-catch GLW signal from an infinite plate.	8
1.7	Actual GLW pitch-catch signal in a complicated structure.	9
2.1	Data collection and image forming process.	14
2.2	Example of the sparse array technique for damage localization.	16
2.3	Experimental setup: (a) Main F/A-18 wing section and blue lab support structure, (b) detailed view of the maintenance access panel with four PZT transducers (T1-T4) bonded to the surface, and (c) schematic cross sectional view of hatch with bolts numbered and units in inches.	19
2.4	Experimentally determined group velocities for the test specimen.	21
2.5	Spatial damage maps (a) TFM image, (b) SCF image, (c) TFM and SCF combined image, and (d) TFM and SCF image with a 60% threshold setting. Black stars are PZT transducers.	24
2.6	TFM images (top) and combined TFM/SCF images with a 60% threshold (bottom) for (a, d) one bolt at 50% torque loss, (b, e) two bolts at 50% torque loss, and (c, f) three bolts at 50% torque loss.	25
2.7	TFM images (top) and combined TFM/SCF images with a 60% threshold (bottom) for (a, c) one group of two at 50% torque loss, and (b, d) two groups of two bolts at 50% torque loss.	28
2.8	Nominal (top) and experimental (bottom) normalized TFM damage images.	31
2.9	Correlation metric, \bar{C} for each bolt number indicating a peak correlation for bolt 5.	32
2.10	Nominal (group velocity adjusted) and experimental (filtered) TFM damage images.	33

2.11	Correlation metric, \bar{C} for each bolt number indicating a peak correlation for bolt 5.	34
2.12	Maxima comparison metric, d_{max} for each bolt number indicating highest correlation (minimum distance between maxima) for bolt 5	35
2.13	Damage cases presented for the blind “technician” survey.	40
3.1	Dual PZT dimensions and signal nomenclature (active PZT elements are darkened)	46
3.2	Signal scaling process for mode decomposition	50
3.3	Demonstration of signal decomposition	50
3.4	Experimentally determined group velocities and theoretical values assuming typical material properties for a 1mm thick Al2024 plate.	53
3.5	Bottom of Piper Cherokee Wing	56
3.6	Design of the sparse array	56
3.7	Sparse PZT array using dual PZT transducers and details of damage inspection area	57
3.8	Plate and transducers used for magnet damage simulation study.	59
3.9	Nondimensional signal amplitude, \bar{A} for a magnet pair and crack	60
3.10	Comparison of baseline subtracted signals for a magnet and crack	60
3.11	Case 1 summation (left) and correlation (right) damage images using the A0 decomposed damage difference signal (top), and S0 decomposed damage difference signals (bottom). The actual damage location is indicated in all images by a star.	66
3.12	Case 2 summation (bottom) and correlation (top) images using the S0 decomposed damage difference signal.	67
3.13	Case 3 correlation damage images using the undecomposed damage difference signal (top) and the decomposed S0 damage difference signal (bottom).	68
3.14	Case 4 correlation damage images using the A0 mode decomposed damage difference signal (top) and the S0 mode decomposed damage difference signal (bottom).	69
3.15	Case 5 correlation damage images using the undecomposed damage difference signal (top) and the S0 mode decomposed damage difference signal (bottom).	70
A.1	79
A.2	Example case	80
A.3	Case 1 - Which bolt is loose?	82
A.4	Case 2 - Which bolt is loose?	83
A.5	Case 3 - Which bolt is loose?	84
A.6	Case 4 - Which bolt is loose?	85
A.7	Case 5 - Which bolt is loose?	86
A.8	Case 6 - Which bolt is loose?	87
A.9	Case 7 - Which bolt is loose?	88

List of Abbreviations

a_{ij}	Instantaneous signal amplitude (envelope)
A	Nondimensional signal amplitude
$A0_{ij}$	A0 mode decomposed signal between transducers i and j
$A_{c,ij}$	Signal scaling factor for A0 mode cancellation for transducer pair (i, j)
$b_{i,j,k}$	Signal polarity for sensor-actuator pair (i, j)
C	Phase velocity
\hat{C}	Maximum of autocorrelation matrix
\bar{C}	Mean of autocorrelation matrix
$\bar{\bar{C}}$	Loose bolt correlation metric
C_g	Group velocity
d_{max}	Distance between maxima of nominal and experimental images
DD_{ij}	Disc PZT i to disc PZT j signal
f	Excitation Frequency
$\mathcal{H}()$	Hilbert Transform
i	Actuator index number
I_{ij}	Damage image matrix
I_{corr}	Correlation algorithm damage image matrix
I_{exp}	Experimental damage image matrix
I_{nom}	Nominal or theoretical damage image matrix
I_{SCF}	Sign coherence factor image
I_{sum}	Summation algorithm damage image matrix
I_{TFM}	Total focusing method image
I_{thresh}	Image threshold level
I_{tot}	Total compounded damage image
j	Sensor index number
N	Total number of sparse array transducers
RD_{ij}	Ring PZT i to disc PZT j signal
s_{ij}	Generic signal of interest between transducers i and j
s_{BL}	Baseline signal
s_{dam}	Damage signal
$S_{c,ij}$	Signal scaling factor for S0 mode cancellation for sensor-actuator pair (i, j)
$S0_{ij}$	S0 mode decomposed signal between transducers i and j
t	Time
t_{ij}	Time of flight for sensor-actuator pair (i, j)
x_{exp}	X coordinate of experimental image maximum
x_{nom}	X coordinate of nominal image maximum
y_{exp}	Y coordinate of experimental image maximum
y_{nom}	Y coordinate of nominal image maximum

σ_k	Standard deviation of signal polarity
A0	Fundamental antisymmetric Lamb Wave mode
CBM	Condition Based Maintenance
CFR	Code of Federal Regulations
DAQ	Data acquisition unit
FAA	Federal Aviation Administration
GLW	Guided Lamb Wave
NAVAIR	Naval Air Systems Command
NDE	Nondestructive Evaluation
NI	National Instruments
NTSB	National Transportation Safety Board
PZT	Lead Zirconate Titanate
SCF	Sign Coherence Factor
SHM	Structural Health Monitoring
S0	Fundamental symmetric Lamb Wave mode
TFM	Total Focusing Method

Chapter 1: Introduction

1.1 Motivation

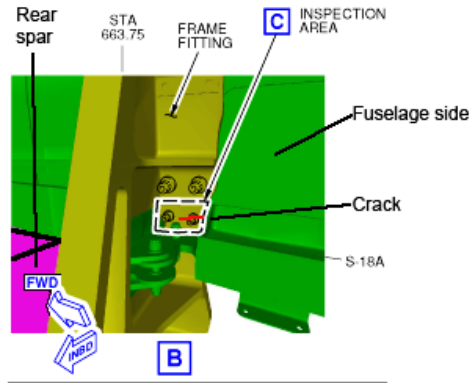
Aviation is one of the safest transportation industries in the United States partially due to the high level of government oversight for maintenance, inspections, and overhauls. In 2017 there were no fatal accidents for carriers operating scheduled flights under 14 CFR 121, and there were only 1.6 non-fatal accidents per million flight hours according to the National Transportation Safety Board (NTSB) [1]. Despite this virtually pristine surface appearance, the aviation industry faces constant problems with fatigue in aging metallic aircraft, especially as both commercial and military operators often seek to extend service lives beyond their original designs. In newer aircraft such as the Boeing 787 which are constructed from a higher amount of composite materials, delamination is more of a concern, and new repair techniques must be developed to address this failure mechanism [2]. Naval aircraft in particular face a unique corrosion problem due to the operating environment in constant saltwater spray [3]. Early detection and tracking of these problems is paramount to maintain high levels of safety throughout aviation.

Current industry practice relies on inspections at established flight hour intervals and replacement and overhaul of parts at similar intervals. Although mostly

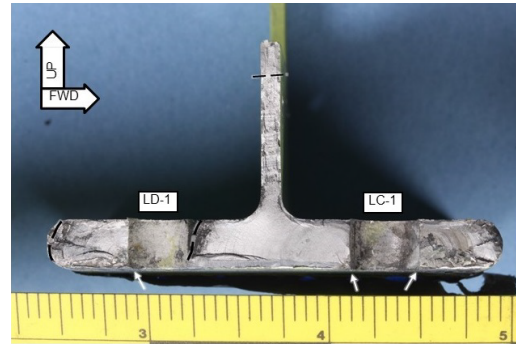
effective, this system is inefficient and prone to failures. Damage often develops which cannot be seen by routine inspections, or it may develop between major inspections. A recent example of this is the discovery of cracked pickle forks on several 737 Next Generation (NG) aircraft. The fatigued part (shown in Fig. 1.1(a) [4]) is critical in load transfer from the wings to the fuselage, and its failure would likely be catastrophic. These cracks were only found during conversion of a high time aircraft to a freighter configuration, and subsequent Federal Aviation Administration (FAA) mandated inspections alerted airlines to more affected aircraft. Another recent example of missed fatigue cracking was a fatal Piper Arrow crash from Embry Riddle Aeronautical university. The NTSB concluded in its report that the accident, which involved separation of a wing during flight, was caused by a large undetected fatigue crack in the main spar (shown in Fig. 1.1(b) [5]). A final recent example was Southwest Airlines Flight 812 which experienced a depressurization event due to fatigue cracking in an incorrectly manufactured fuselage section (shown in Fig. 1.1(c) [6]). Because the inspection system is prone to failure, enhancements which improve safety are justifiably necessary. The following section discusses the field of structural health monitoring (SHM) and ways in which it intends to address gaps in the current aircraft maintenance system.

1.2 Structural Health Monitoring

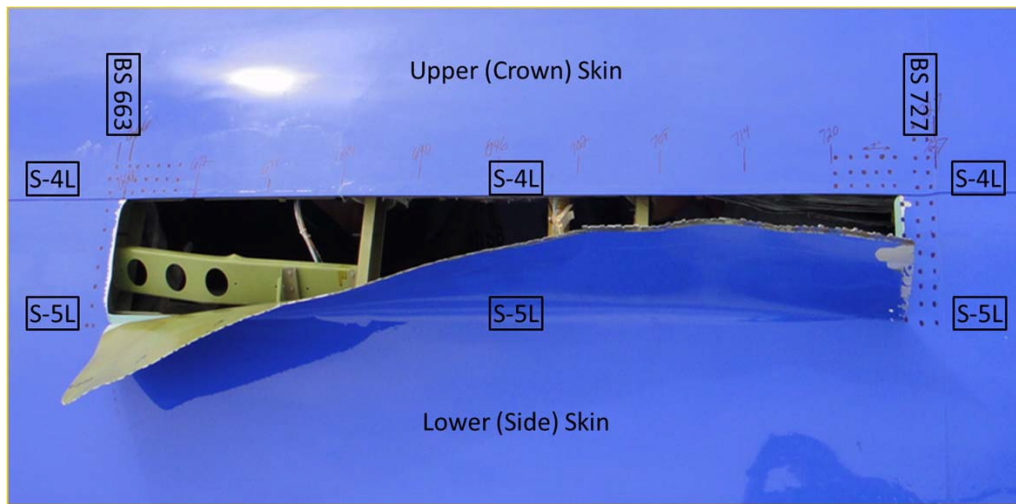
SHM is a diverse field which seeks to develop systems for structures which are capable of detecting and diagnosing damage, as well as calculating the remaining



(a) Boeing 737NG pickle fork cracks



(b) Piper Arrow spar fatigue failure



(c) Southwest Airlines Flight 812 Depressurization

Figure 1.1: Aviation fatigue examples and incidents.

life available for system components. In an ideal scenario, SHM would improve the safety, reliability, and efficiency of aeronautical maintenance practices by providing precise tracking of component damage without the need for constant routine inspections by technicians. In the near term, SHM will act as a supplement to mandatory inspections preventing missed damage between inspections and allowing for damage tracking in difficult to inspect parts of aircraft structures. In the long term, the goal for SHM is to achieve condition based maintenance (CBM), a system which emphasizes the precise tracking of part life based on SHM-determined condition

and replacement near the actual end of a part’s life rather than after surpassing a predetermined lifetime measured in hours [7]. Such a system would reduce aircraft downtime, improve the cost effectiveness of maintenance, and prevent both wasted part life and unexpected premature failures. SHM methods have been subdivided into four levels by Rytter [8]. These levels were established to categorize SHM techniques based on the extent of their capabilities. An SHM classification system based on the Rytter system is presented in table 1.1.

Table 1.1: SHM Classification Levels

Classification	Title	Description
Level I	Detection	Provides an indication that damage is present.
Level II	Localization	Provides a possible location for the damage.
Level III	Assessment	Quantifies the size and extent of the damage.
Level IV	Prognosis	Assesses system safety and remaining life.

The work in this thesis focuses on levels I,II, and III, with a particular focus on level II (localization). This work also focuses on a specific group of SHM techniques that make use of ultrasonic guided Lamb Waves (GLW). Background on Lamb Waves is presented in the following section.

1.3 Guided Lamb Waves

Lamb Waves, guided plate waves, or guided Lamb Waves (GLW) are a type of ultrasonic plate vibration guided by the free surfaces of a plate (the waveguide). Lamb Wave behavior consists of both flexural and axial displacement, and the waves can be divided into symmetric and antisymmetric modes. The presence of these modes and their dispersive properties such as wave speed (phase velocity) are a

function of their frequency and the thickness of the plate. Phase velocity, C , is the speed at which the phase of a wave propagates through space. A similar dispersion property, the group velocity, C_g , is the speed at which the envelope of a wave packet propagates through space. At most relatively low frequency-thicknesses of interest (< 1.0 MHz-mm in aluminum), only the fundamental symmetric (S0) and fundamental antisymmetric (A0) modes can be excited. In this domain the S0 mode is mostly nondispersive, meaning that waves of different frequencies propagate at the same speed. This also implies that the phase velocity is approximately the same speed as the group velocity. In the low frequency-thickness domain, the S0 mode approaches the behavior of an axial wave. In contrast, the A0 mode is highly dispersive and its behavior resembles a mostly flexural wave in the low frequency-thickness domain. Figure 1.2 shows the phase and group velocity (dispersion curves) of the fundamental Lamb Wave modes in a 1mm thick Al2024-T3 plate for frequencies below 500 kHz. The phase velocity can be determined numerically by solving the Rayleigh-Lamb equation which is a function of frequency-thickness. Group velocity can then be derived through a simple relation to phase velocity [9]. Figure 1.3 demonstrates the dispersion principle and shows that physically, the shape of the dispersive A0 mode changes as it propagates through the waveguide. Particularly, high frequency parts of the wave packet propagate faster than the low frequency parts causing the packet to spatially disperse.

For SHM, GLWs are useful because if the waves encounter a nonlinearity in the structure such as a crack, then a reflected or scattered wave is produced. In theory, by detecting this reflected wave, one can declare that damage is present in a struc-

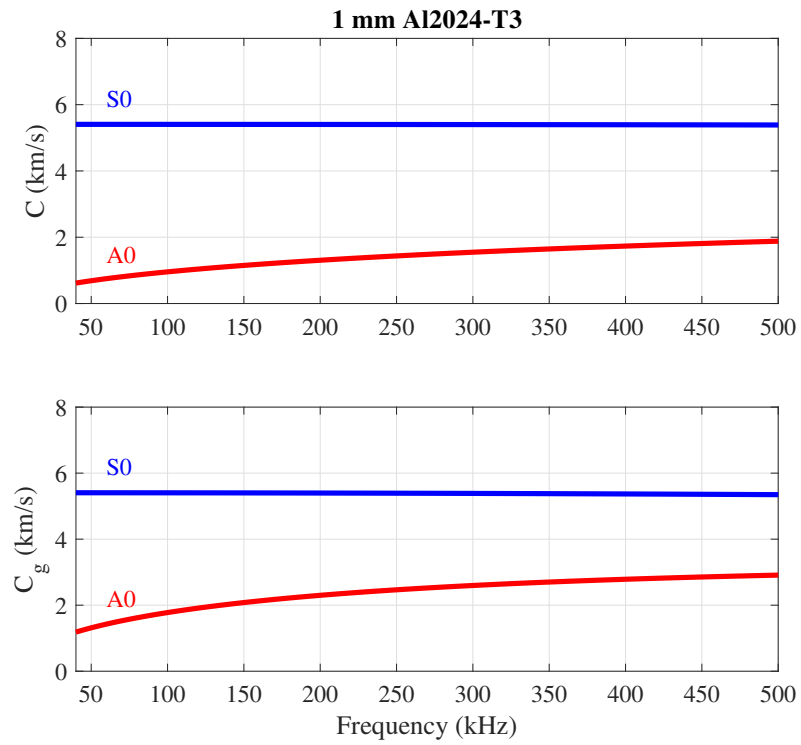


Figure 1.2: Dispersion curves for Al2024-T3 with thickness 1 mm.

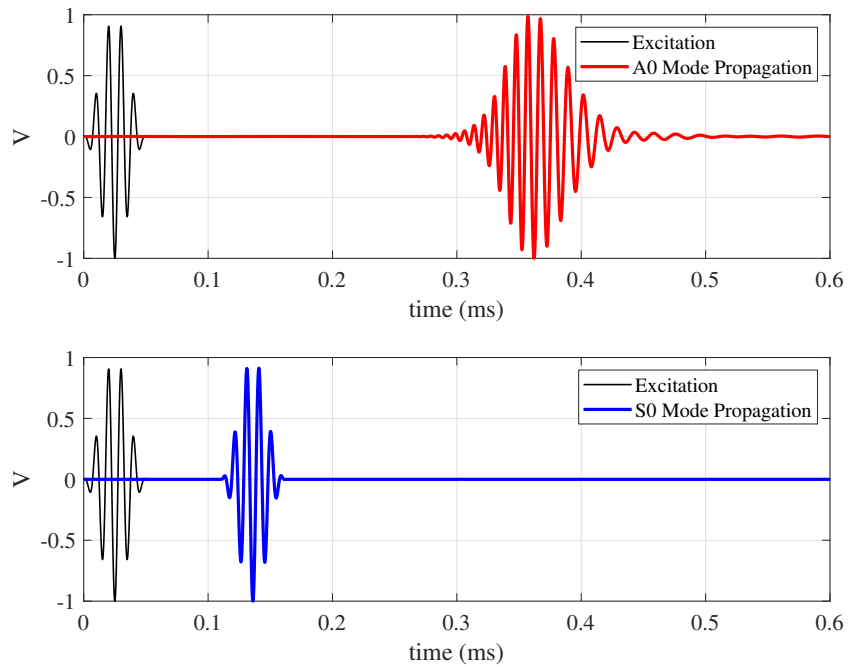


Figure 1.3: A0 and S0 modes 600 mm from a 100 kHz 4.5 cycle excitation in Al2024-T3 with thickness 1 mm.

ture, and with certain transducer setups, one can even determine the location of the damage based on the group velocity of the mode of interest. Figure 1.5 demonstrates the pitch-catch technique for measuring reflections where one transducer is used to excite the plate and another is used to measure the response at another location in the plate. Piezoelectric materials such as Lead Zirconate Titanate (PZT) are often selected as transducers due to their small form factor, simple operation, and high electroacoustic efficiency [9]. When an electric field is applied to a piezoelectric material such as PZT, the material strains which is then transferred to the plate it is bonded to (converse effect). The opposite effect (direct effect) implies that application of strain to the PZT produces an electric field [10]. These effects allow piezoelectric materials to be used as both actuators and sensors respectively. The size of the piezoelectric wafer as well as the frequency of excitation determine the tuning curves for the fundamental Lamb Wave modes (example shown in Fig. 1.4). These curves predict the normalized amplitude of each mode and allows one to tune a response to excite mostly a single dominant mode if desired [9]. Fig. 1.6 shows an ideal pitch-catch signal from the sensor shown in Fig. 1.5. Here the reflected wave due to damage is clearly visible in the sensor signal.

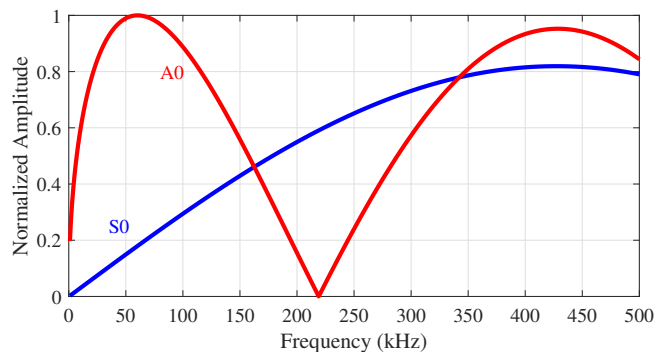


Figure 1.4: Tuning curves for 1mm thick Al2024-T3 and 6.3 mm dia. PZT

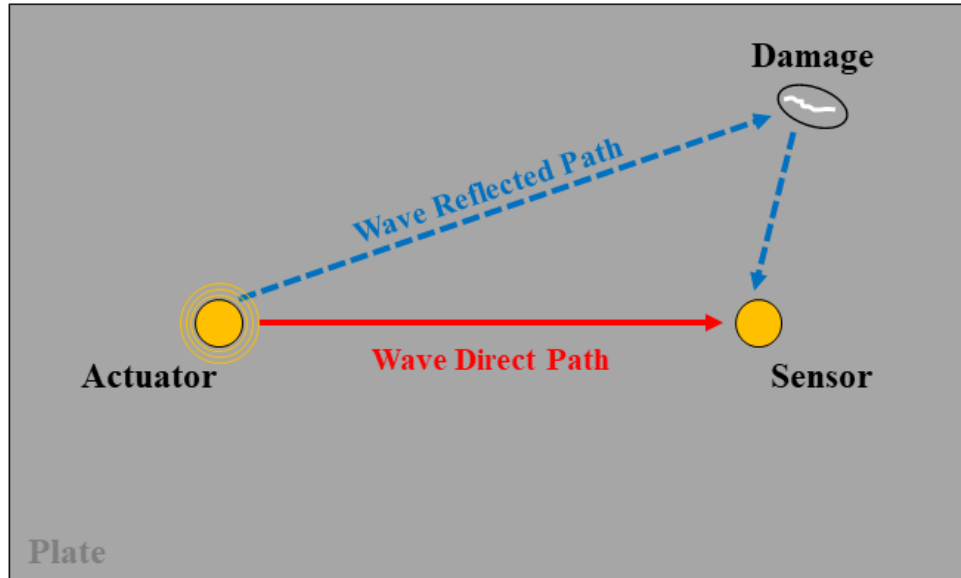


Figure 1.5: GLW pitch-catch propagation in a plate.

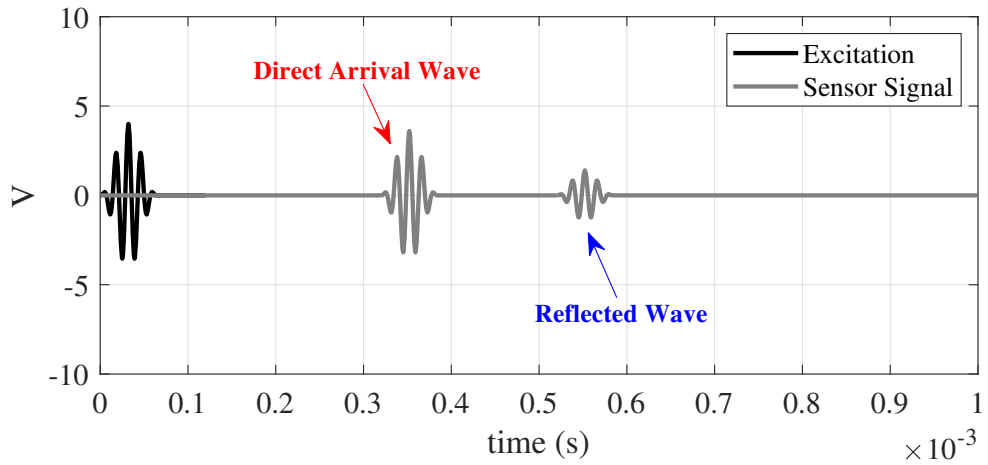


Figure 1.6: Ideal single mode, nondispersive pitch-catch GLW signal from an infinite plate.

In practice applying this damage detection principle is much more involved due to the very same behavior that allows damage detection in the first place. Specifically, GLWs also reflect when they encounter, rivets, plate edges, plate stiffening features, and any other complicated features in a structure. Moreover, without careful design and tuning, often both the A0 and S0 mode are excited by PZT actuators. Signals are further complicated by the principle of mode conversion in which a single mode interacts with a structural nonlinearity and is converted into both the A0 and S0 mode when it is reflected. Thus, a pitch catch signal in an actual structure is significantly more difficult to interpret as shown by Fig. 1.7.

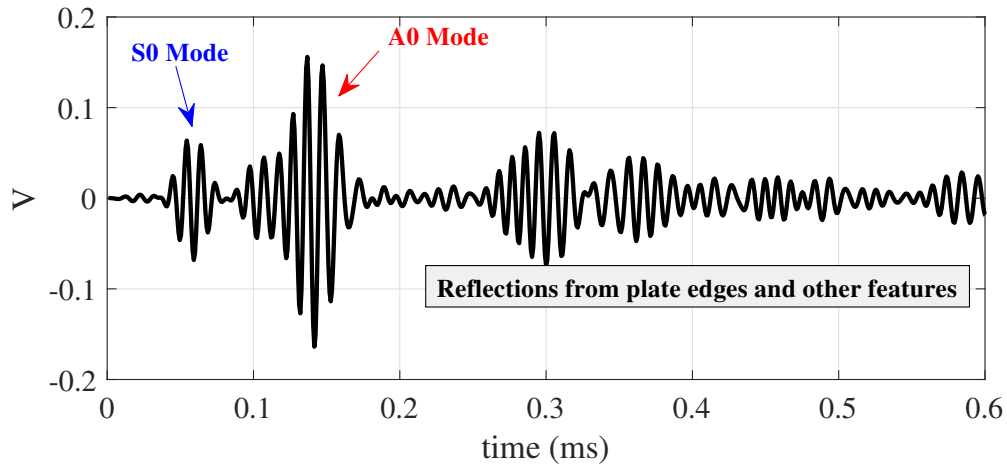


Figure 1.7: Actual GLW pitch-catch signal in a complicated structure.

1.4 Scope of Thesis

Guided Lamb Waves have been extensively explored for a variety of SHM applications as will be presented in the introductions of the following chapters. Despite this extensive work, GLW SHM techniques have not been readily accepted by the aviation industry for any practical applications. This is partially due to the

fact that much work has remained at the basic research level, and more studies are needed which involve actual, complicated aircraft structures. In an effort to address these concerns, this thesis was divided into the following two case studies which each investigate several aspects related to practical deployment of GLW SHM techniques:

1. F/A-18 wing torque loss monitoring

- Apply GLW SHM techniques to a complicated composite structure, and study the system's ability to produce spatial damage maps. Identify any challenges or deficiencies.
- Evaluate several options for autonomous torque loss detection and localization.
- Study human factors related to interpretation of SHM data.

2. Piper Cherokee wing damage localization

- Study the influence of complex structural features on GLW technique performance.
- Apply a nontraditional dual element PZT transducer to decompose GLW signals into the constitutive A0 and S0 modes.
- Evaluate the mode decomposition technique for practical aircraft SHM applications, and determine if performance improvements are realized.

Chapter 2: F/A-18 Wing Torque Loss Monitoring

2.1 Introduction

Guided Lamb Waves (GLW) have been demonstrated as an effective ultrasonic tool for damage detection and localization due to their scattering upon interaction with nonlinearities such as cracks. Various GLW methods have been developed [11, 12], and they have been explored for their potential application in complex aerospace structures to detect and localize cracks, holes, torque loss in bolts, and material loss due to corrosion [13–17]. Dalton et al. [18] in particular investigated structural features common to aircraft such as lap joints and doublers and concluded that propagation of GLWs over distances greater than 1 m was not feasible due to signal attenuation from bonding layers. This leaves GLWs appropriate for smaller structurally significant locations in the near term for structures with significant attenuating features. GLW localization algorithms making use of piezoelectric arrays are found in compact, high density (for tomography), and sparse forms [19]. Sparse arrays are ideal for monitoring the largest possible area with minimal sensors and simple localization algorithms [20] which makes them a natural choice for aircraft structures.

Ideal SHM is meant to eliminate human factors such as manual inspection

through entirely autonomous algorithms [21], but humans are presently still better at performing certain tasks such as pattern recognition. An example of this is the prevalence of CAPTCHAs to deter malicious bots on websites [22]. Although research into computer pattern recognition (machine learning) is proving successful in some cases (even for CAPTCHAs [23]), for full scale aircraft SHM, machine learning is presently impractical due to the need to generate damage training cases for damage localization [24]. Thus, humans are at least in the foreseeable future a necessary part of any substantial SHM system, particularly for interpretation of damage localization data in complicated damage cases. Some works have investigated human interaction with non destructive evaluation (NDE) [25–27], but bridging the creation of new SHM techniques and practical application requires further contributions in this topic.

This chapter presents a practical case study for an SHM scenario by applying a GLW damage localization technique to a panel on a legacy F/A-18 composite wing. The applied technique is described in detail, and results to various simulated damage cases are discussed. Autonomous methods of interpreting these images are explored, and ultimately a blind study involving human data interpreters is presented. Challenges in applying GLW techniques to complex real aircraft structures are discussed, and the need to analyze SHM techniques from a human factors perspective during development is emphasized.

2.2 Guided Lamb Wave Damage Localization Techniques

The basis for GLW damage localization schemes revolves around measuring scattering from damage, and distinguishing this from scattering due to structural complexities such as plate edges and rivets. In the present case, to measure the scattering from induced damage, baseline signals are recorded between each sensor-actuator pair in a four element sparse array. Subsequently, these baselines are subtracted from signals recorded at a later point with damage potentially present. Baseline subtraction requires control of temperature during measurement, or several baselines must be collected at differing temperatures. Despite this, baseline subtraction is advantageous in providing good localization capability in complicated structures. The envelope of the scattered signal is measured using a Hilbert transform, and a time of flight calculation is performed. This enables mapping from the time domain of the scatter signals to the space domain of the inspection area around the sparse array. Specific to this work, an image compounding technique is described to form the spatial damage maps by combining two types of images (TFM and SCF). An overview of the construction of these images is presented in Fig. 2.1 and is explained in detail in the following section.

2.2.1 Total Focusing Method (TFM)

The main localization scheme used in this work involves an image compounding technique using both GLW signal amplitude and phase information. [20, 28, 29], describe the process of forming these images, but the formulae are explained below,

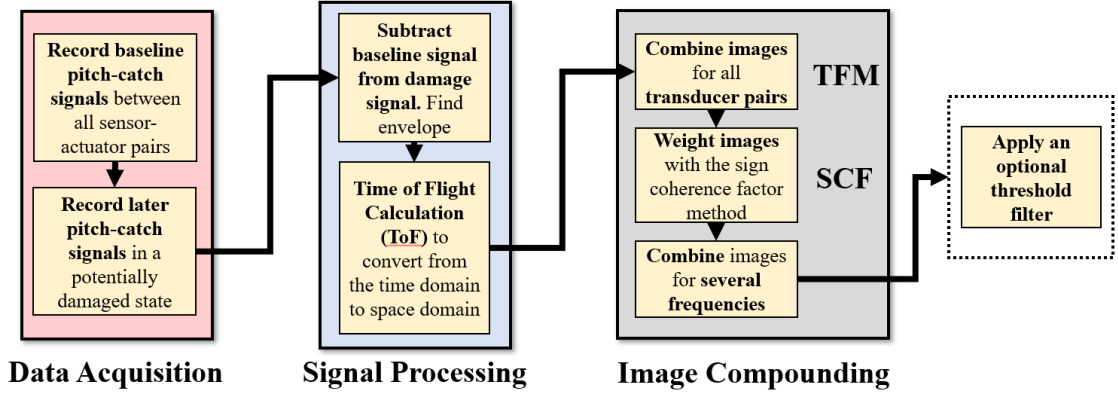


Figure 2.1: Data collection and image forming process.

as some modifications were made from these papers for the sign coherence factor (SCF) image. First, the TFM image using damaged signal amplitude information is formed by

$$I_{TFM}(f, x, y) = \frac{1}{N(N-1)} \sum_{i=1}^N \sum_{j=1}^N a_{ij(i \neq j)} \left(t_{ij}(f, x, y) \right) \quad (2.1)$$

where the instantaneous amplitude signal of sensor measurements, can be given using a Hilbert transform, of the signal, $s_{ij}(t)$ as below

$$a_{ij}(t) = |s_{i,j}(t) + i\mathcal{H}[s_{i,j}(t)]| \quad (2.2)$$

As stated, a baseline differenced signal was required for the signal $s_{ij}(t)$. The time-of-flight among the transmitting PZT i , the imaging point (x, y) , and the receiving PZT j can be determined by

$$t_{ij}(f, x, y) = \frac{\sqrt{(x-x_i)^2 + (y-y_i)^2} + \sqrt{(x-x_j)^2 + (y-y_j)^2}}{C_g(f)} \quad (2.3)$$

where $C_g(f)$ is the group velocity of a selected wave mode with a given excitation frequency (f), which is experimentally determined as described below. Note that the fundamental antisymmetric mode (A0 mode) was used for this work because this particular Lamb wave mode was dominant in the relatively low excitation frequency range of 40-100 kHz for guided Lamb wave interrogations. The A0 mode with a slow propagation speed was identified from a series of experimental measurements using individual sensor networks of the sparse array. The fundamental symmetric mode (S0 mode) was also identified, but it was substantially weaker than the A0 mode. The presented technique is sometimes referred to as the sparse array imaging technique since it makes use of a sparse transducer array and uses a basic triangulation-like technique to determine a probable location of damage. Figure 2.2 presents a visualization of the sensor-actuator space domain conversion which forms several intersecting ellipses to localize potential damage.

2.2.2 Sign Coherence Factor (SCF) Imaging

The second half of the image compounding technique uses damaged GLW signal phase information to construct the SCF image. This image functions primarily as a weighting factor for the TFM image, improving its contrast and removing locations of false damage indications. The SCF image is given by

$$I_{SCF,k}(f, x, y) = 1 - \sigma_k \quad (2.4)$$

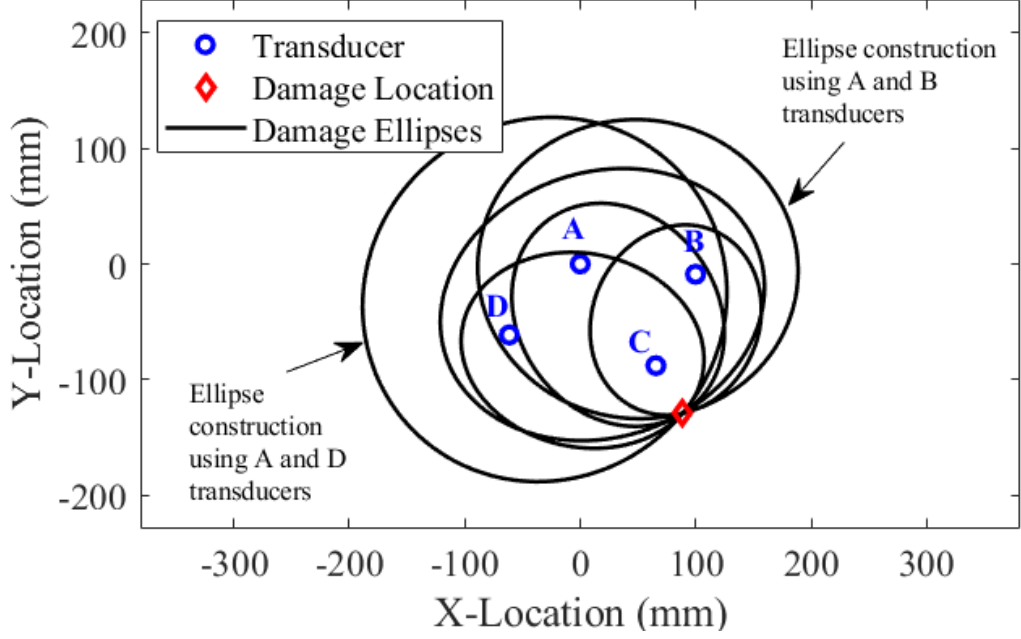


Figure 2.2: Example of the sparse array technique for damage localization.

$$\sigma_k^2 = 1 - \left[\frac{1}{N(N-1)} \sum_{i=1}^N \sum_{j=1}^N b_{i,j,k,(i \neq j)} \left(t_{ij}(f, x, y) \right) \right]^2 \quad (2.5)$$

For this work, the polarity or algebraic sign $b_{i,j,k}(t)$ was divided into two elements slightly modified from the equations shown in [28], [29].

$$b_{i,j,k}(t) = \begin{cases} 1 & \text{if } s_{i,j}(t) \geq 0 \\ 0 & \text{if } s_{i,j}(t) < 0 \end{cases} \quad \text{for } k = 1$$

$$b_{i,j,k}(t) = \begin{cases} 0 & \text{if } s_{i,j}(t) \geq 0 \\ -1 & \text{if } s_{i,j}(t) < 0 \end{cases} \quad \text{for } k = 2$$
(2.6)

The combined array images were evaluated by multiplying the imaging results from the TFM and SCF signal processing algorithms:

$$I(f, x, y) = \frac{1}{2} \sum_{k=1}^2 I_{TFM}(f, x, y) \cdot I_{SCF,k}(f, x, y) \quad (2.7)$$

The final array images for this work were determined by integrating all combined array imaging results with various excitation frequency cases, given by

$$I_{tot}(x, y) = \frac{1}{M} \sum_{f=f_1}^{f_M} I(f, x, y) \quad (2.8)$$

In some cases an additional threshold filter is desired to improve the contrast of the combined TFM/SCF image. This threshold is defined by

$$I_{tot}(x, y) = \begin{cases} I_{tot}(x, y) & \text{if } I_{tot}(x, y) \geq I_{thresh} \\ 0 & \text{if } I_{tot}(x, y) < I_{thresh} \end{cases} \quad (2.9)$$

The threshold filter level would in practice be optional and adjusted by a technician reviewing the data for their preference in interpreting data.

2.2.3 Experimental Setup

The test specimen for this study is a section of a legacy F/A-18 composite wing skin provided by the Naval Air Systems Command (NAVAIR). Particularly, the focus of this study is a maintenance access panel secured to the main wing structure via twenty fasteners. This panel is a composite ellipse of unknown material

properties, but it is assumed to be a typical quasi-isotropic laminate structure. The panel is approximately 7 mm thick bolted flush to a larger composite skin section about 20 mm thick. The mounting portion of the thick composite skin is formed by an ellipse offset by 38 mm from the panels outer edge. Figure 2.3 shows the details of the panel geometry and cross section. As previously discussed, complex structures often pose challenges in using the GLW method due to the complexity of the signals, but this test specimen posed other challenges due to the relatively thick construction and high structural damping. The original flush fasteners installed on this panel were replaced with more standard hex head bolts for ease in manipulating the torque specifications of each bolt. A spatially distributed array of four 6.35 mm diameter PZT-5A wafers were permanently bonded to the surface of this panel in a semi-random pattern after the surface was locally stripped of all layers of paint. This sparse array allows for surveying of a large area with only a few sensors - ideal for an aircraft structure where minimalism is a necessity. Some array design criterion considered for ideal signal quality are the semi-random spacing between PZT elements and sufficient offset from panel edges to avoid signal cluttering from panel edge reflections. Although the array configuration was not strictly optimized, it was constructed to provide coverage for all bolts on the panel with a minimum number of transducers. This array configuration yields six unique sensor-actuator pairs to be used when integrating a spatial damage map.

For all damage trials, an initial baseline set of data was recorded, after which simulated damage was imposed on the structure and all data was collected again. For each case, and each sensor-actuator pair, one designated transducer emitted

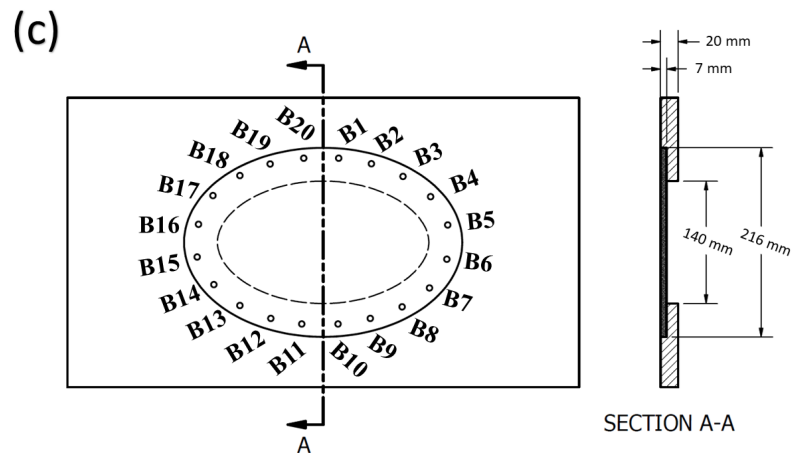
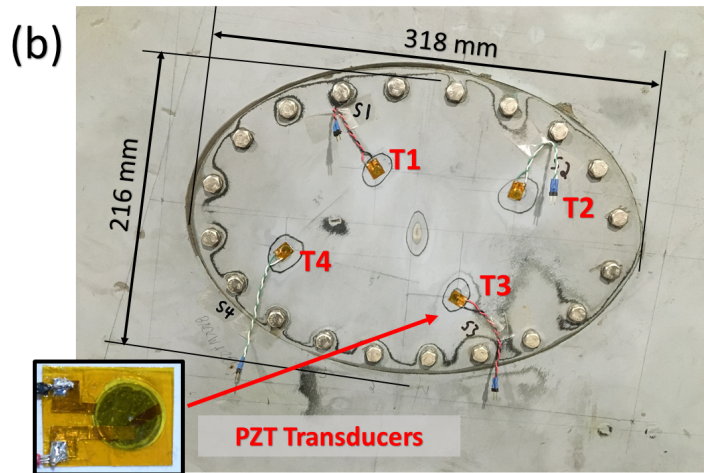
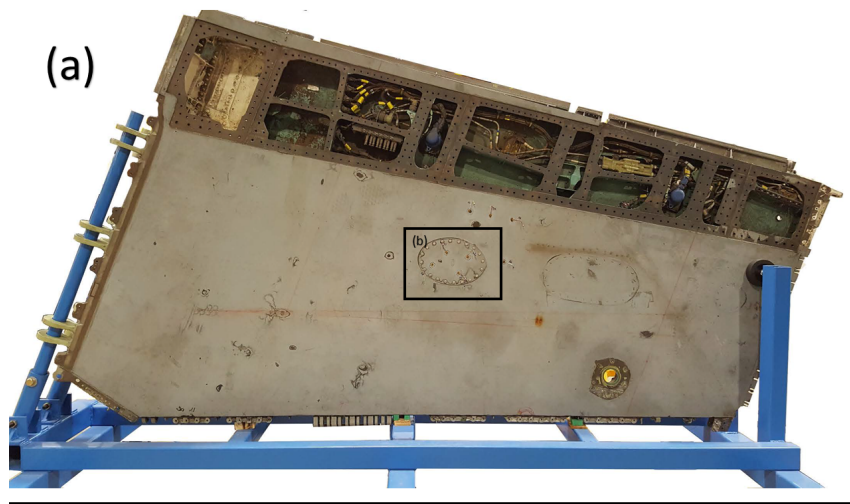


Figure 2.3: Experimental setup: (a) Main F/A-18 wing section and blue lab support structure, (b) detailed view of the maintenance access panel with four PZT transducers (T1-T4) bonded to the surface, and (c) schematic cross sectional view of hatch with bolts numbered and units in inches.

the 160V peak to peak excitation signal generated by an NI USB DAQ and linear amplifier, while the other transducer recorded the structural response at a sample rate of 1.25 MHz in groups of 2500 samples. Responses were recorded through a range of actuation frequencies between 40 kHz and 100 kHz with each sensor-actuator coupling. Lower excitation frequency responses generally exhibited a higher signal to noise ratio, less initial EMI, higher resolution, and less modal interference, so frequencies greater than 100 kHz were not used for these studies. A multiplexer is often used to cycle through each sensor-actuator combination, but in our case with only six unique pairs, a manual method was preferred to avoid the introduction of phase shift often present with multiplexing. High frequency noise was reduced through ensemble averaging of 100 signals per case, and the signals were filtered in post processing through a 4 pole low pass Butterworth filter.

In order to transform the time domain Lamb wave responses to space domain images using the TFM and SCF methods, approximations of the group velocities for the fundamental modes were needed. These approximations were obtained based on average arrival time measurements for each sensor-actuator pair and the known geometry of the PZT array. The equation for the approximated group velocity is given by

$$C_g(f) = \frac{1}{N(N-1)} \sum_{i=1}^N \sum_{j=1}^N \frac{\sqrt{(x_j - x_i)^2 + (y_j - y_i)^2}}{(t_{a,i,j}(f) - t_{c,i,j}(f))} , \quad i \neq j \quad (2.10)$$

where $t_{a,i,j}$ is the arrival time of the mode of interest, and $t_{c,i,j}$ is the center time of the excitation toneburst. Although the GLW signals were complex due to the

inhomogeneous nature of the aircraft structure, both the A0 and S0 mode were identifiable. As mentioned previously, the signals were assumed to consist of solely the A0 mode as an appropriate simplification because of the mode's dominance. To be thorough Fig. 2.4 shows the measured group velocities of both the fundamental A0 and S0 modes in the range of excitation frequencies used (40 kHz-120 kHz).

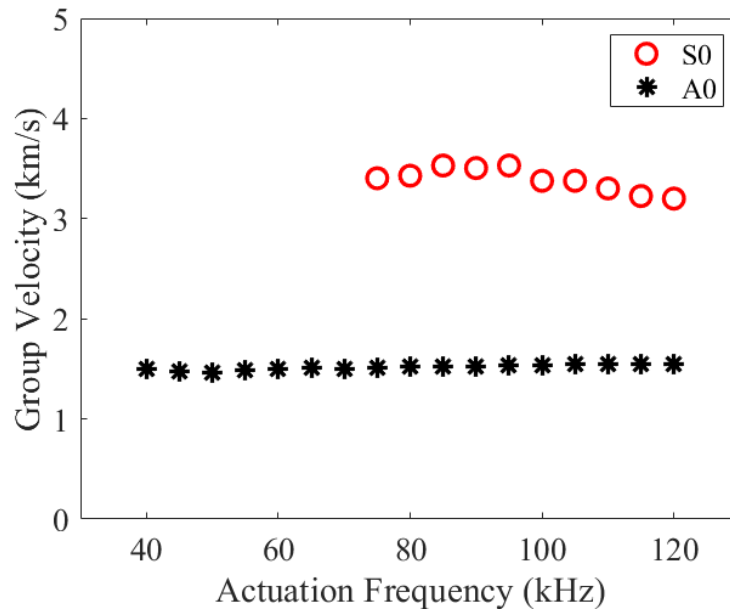


Figure 2.4: Experimentally determined group velocities for the test specimen.

2.3 Damage Detection Image Results

The following sections present and analyze sample damage images using the techniques described in the previous section. Damage imparted on the test specimen was torque loss to the panel's surrounding fasteners. For each case study, all bolts were initially set to a reference torque setting of 6.78 Nm (60 in-lbf), and baseline measurements were recorded. The relatively loose torque specification of 6.78 Nm was selected to minimize relaxation over time and to assess the sensitivity of the

system to small torque changes. A brief investigation showed that any bolt relaxation within the first 24 hours of installation was negligible, so that all subsequent studies could be performed over an extended period of time if necessary. For each study, frequencies between 40 and 100 kHz were used to construct the spatial damage images. The first torque loss study tested the image compounding technique for a single loose bolt on the panel. The goal of this was to develop an understanding of the amount of torque loss and loose bolts required to be seen by the image compounding technique. The next study examined torque losses of 50% in groups of 1 to 3 bolts in order to study the effects of growing damage levels in localized sections of the panel. Finally, damage was distributed throughout the panel with 50% torque loss in multiple groups of bolts with the intention of characterizing the image compounding technique's ability to identify multiple damage locations.

2.3.1 Single Bolt Torque Loss Images

In the first study, bolt 10 (B10 in Fig. 2.3) was loosened until it could clearly be seen by the TFM, and compounded damage images. At torque losses below about 38%, use of the image compounding technique was not effective since the resulting images from these low torque losses showed poor contrast due to the relatively small differences between the baseline and damaged signals. The image compounding damage localization technique presented meaningful results at higher torque losses such as 50%. Fig. 2.5 shows the image compounding process referenced by Eq.2.7 for the single bolt (B10) at 50% torque loss. In this case the GLW signal amplitude

information used by the integrated TFM method was sufficient to localize damage to the lower section of the panel as shown in Fig.2.5(a). However, the combination of the integrated TFM and SCF images yielded an image with maximum damage levels almost precisely at location of the loosened bolt - B10 (Fig. 2.5(c)). A 60% threshold significantly improved the contrast of the final image shown in Fig.2.5(d), clearly demonstrating that damage to the structure originated at the bolt B10. This study shows that for a single loose bolt greater than 38% torque loss, damage is clearly and accurately visible on the TFM and combined threshold images.

2.3.2 Single Group Torque Loss Images

The second study examined the use of the TFM and compounded image techniques to study growing torque loss damage in a single group of bolts. Fig. 2.6 shows these images for the three steps of damage simulated for this study. The damage progression from left to right in the figure starts with B10 loosened to 50% torque loss, followed by the addition of B11, and finally by the addition B12 to form a group of three loosened bolts. The integrated TFM images shown in the top row of Fig. 2.6 clearly demonstrate growing damage levels in each case when presented at the same scale. In general though, damage localization is not as focused at the higher damage levels with the TFM image. The compounded TFM and SCF images with 60% threshold shown in the lower row of Fig. 2.6 also clearly demonstrate growing damage levels, although the localization shows higher contrast than the TFM images alone. Damage growth is characterized here by a growing region of indicated

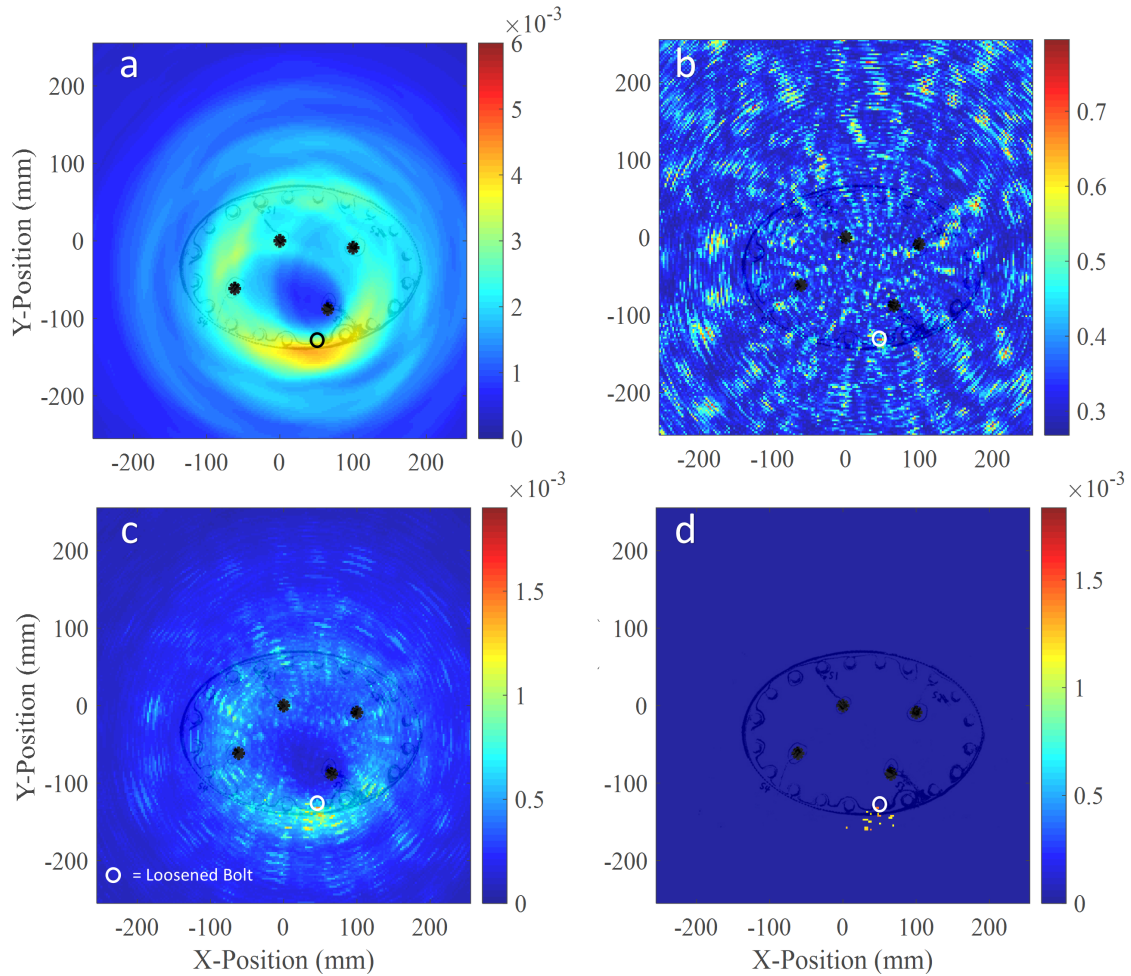


Figure 2.5: Spatial damage maps (a) TFM image, (b) SCF image, (c) TFM and SCF combined image, and (d) TFM and SCF image with a 60% threshold setting. Black stars are PZT transducers.

damage in the lower section of the panel and an increasing image maximum damage level. More image artifacts are present at the higher damage level mostly due to the dominance of the lower PZT pair (T3-T4) in the image compilation, but the main concentration of damage is still clear with this compounded image. A user of this SHM system would likely know in these cases that a loose bolt is present in the lower half of the panel, although it would be more difficult to determine the exact loose bolts from looking at these images.

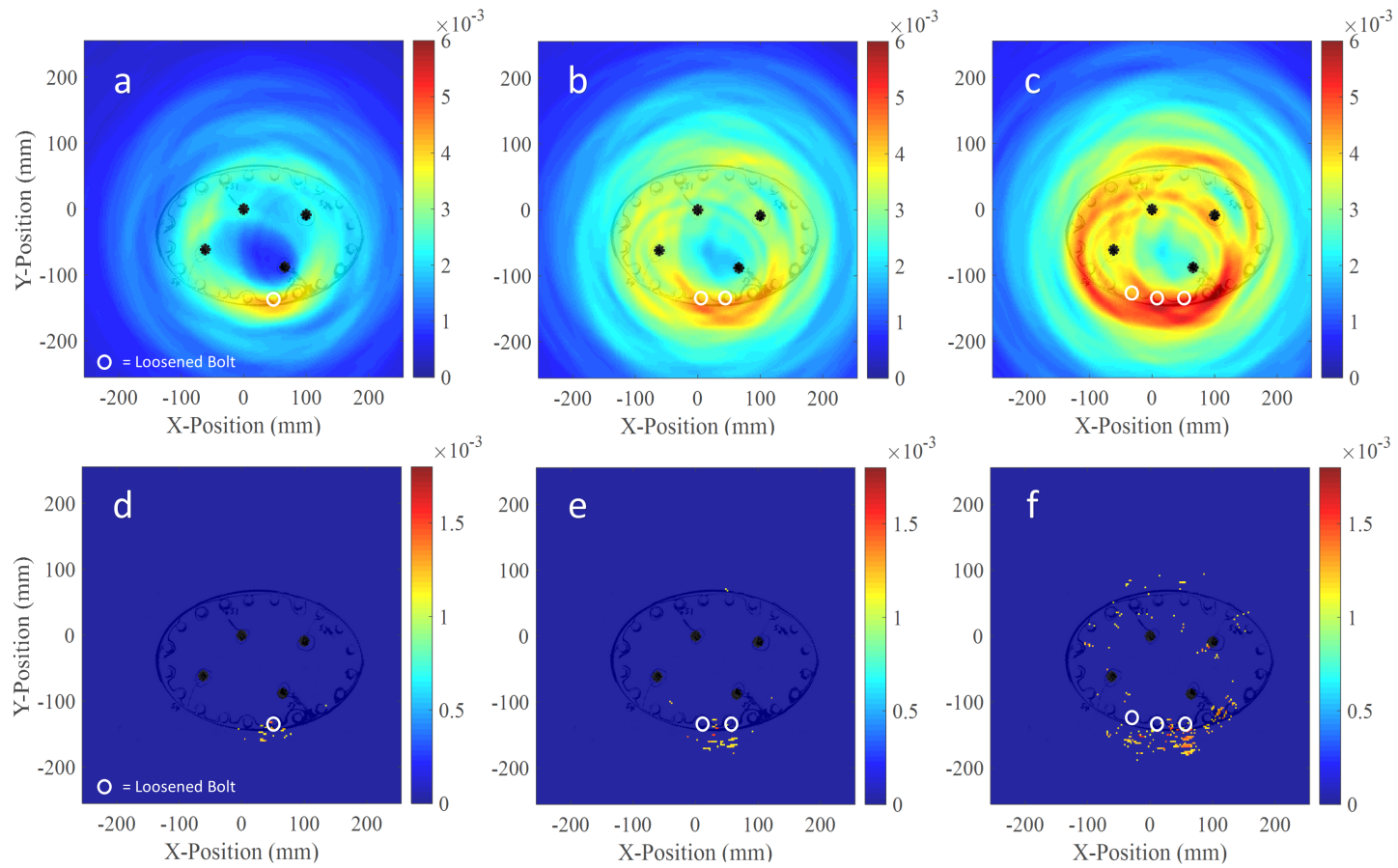


Figure 2.6: TFM images (top) and combined TFM/SCF images with a 60% threshold (bottom) for (a, d) one bolt at 50% torque loss, (b, e) two bolts at 50% torque loss, and (c, f) three bolts at 50% torque loss.

2.3.3 Multiple Group Torque Loss Images

The final damage study examined a case with damage present in two separate locations on the panel. This study was intended to assess the damage image results in a realistic case where damage is not confined to one location. Fig. 2.7 shows the integrated TFM and compounded 60% threshold images for two damage cases. Damage to the groups was induced in two steps - first a group of lower section bolts (B11 and B12) were loosened by 50% followed by a case with two additional bolts loosened in the upper quadrant of the panel (B1 and B2). For the first single group case, the TFM image shows damage in the lower sections of the panel, but the dominance of the T3-T4 PZT pair reduces the clarity of the image (Fig. 2.7(a)). The TFM method is even less effective with the multiple group damage case due to the overlapping dominant pairs T1-T2 and T3-43 which presents multiple false damage locations (Fig. 2.7(b)).

The damage locations cannot be deduced from this image due to the lack of clarity using TFM alone. The dark red areas of likely damage are spread over most of the panel boundary leaving one only able to say definitively that a bolt is loose in several places on the panel. The compounded TFM and SCF images for each case greatly improves the contrast when combined with a 60% threshold making localization easier for both cases (see Fig. 2.7(c,d)). This method particularly improves the case with damage present in two separate quadrants of the panel, as the previously shown false damage locations from the TFM image were eliminated for the most part. However the image still favors the upper group of loose bolts and

may cause one to overlook the loose bolts at the bottom of the panel.

Some artifacts are present in the final compounded images due to the dominant transducer pairs in the underlying TFM image, however the main damage is still clearly identifiable. It should also be noted that damage throughout all studies often presented itself just outside of the panel edge rather than at the loosened bolts. This is most likely attributed to the inhomogeneous nature of the structure and in particular, the varying thicknesses between the panel and its mount as well as the differing composite materials in these two parts of the structure. These factors render the constant group velocity assumptions used in this chapter somewhat inaccurate and could contribute to the slightly displaced damage indications. Regardless, the combined TFM and SCF images provide sufficient localization capability to confine damage to a particular set of bolts or quadrant of the panel. It is clear that this particular application of the image localization schemes is likely not ideal due to the complexity and thickness of the structure and the constraints of the transducer array. Results achieved here were not comparable to the ideal cases found in the original studies using simple aluminum plates.

2.4 Autonomous Damage Detection

2.4.1 Image Cross-Correlation

In order to interpret the damage images like those generated in the previous section, autonomous damage detection algorithms were explored. The first makes use of image cross correlation to determine if a bolt is likely to be loose. For

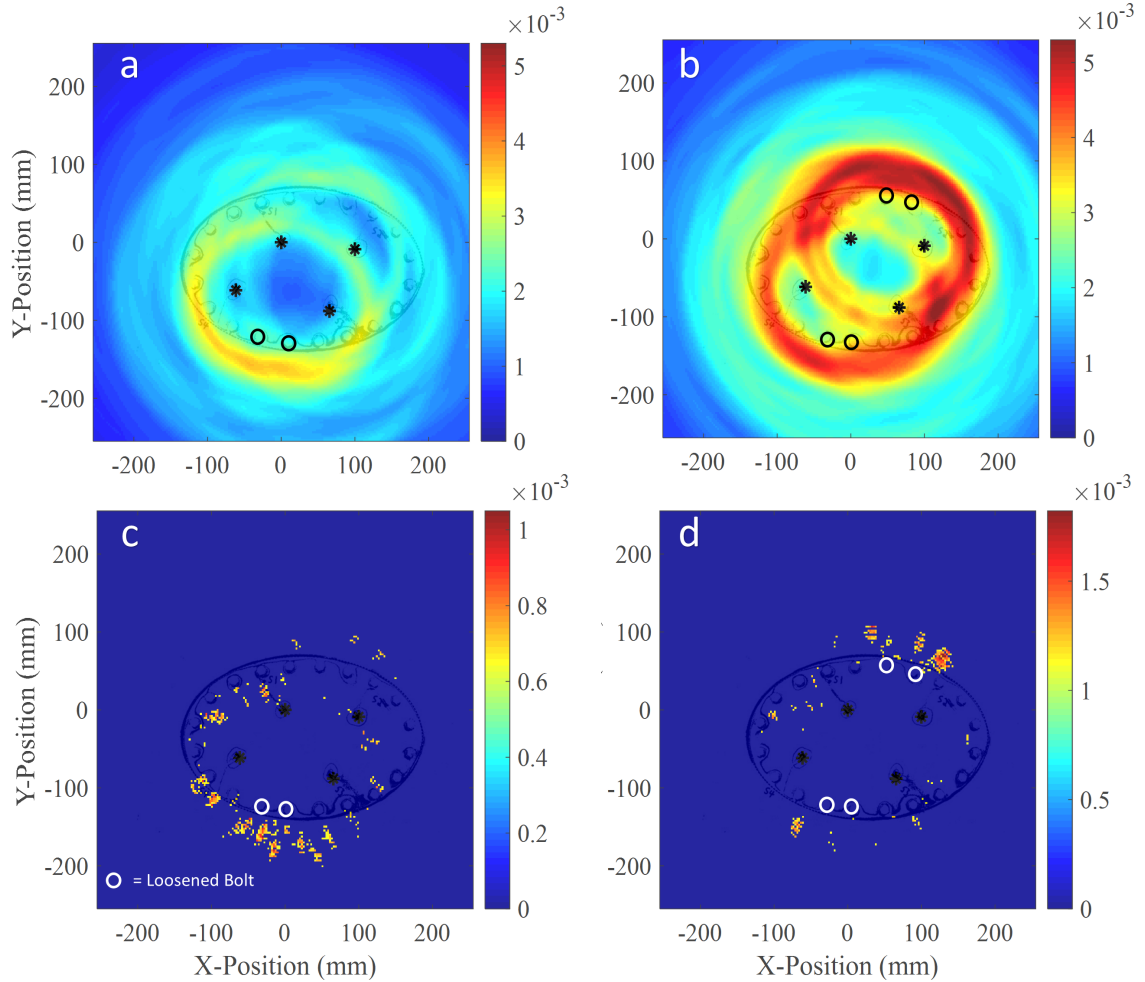


Figure 2.7: TFM images (top) and combined TFM/SCF images with a 60% threshold (bottom) for (a, c) one group of two at 50% torque loss, and (b, d) two groups of two bolts at 50% torque loss.

this method, “nominal” or “theoretical” TFM damage images are compared to the experimentally constructed images to determine the closest matching loose bolt. These nominal images are generated for each all 20 bolts in the panel of interest. To generate these images, an ideal difference signal was constructed using a Gaussian windowed envelope with its center at the corresponding time of flight for each sensor actuator pair, bolt number, and excitation frequency combinations. Converting these ideal signals to TFM images yields the nominal or theoretical image for each

bolt number. For any given experimentally generated TFM image, cross-correlation was performed to compare this image with each of the 20 nominal damage TFM images. Interpretation of the cross-correlation is determined by measuring certain properties of the auto-correlation matrix which is defined here.

$$C(k, l) = \sum_{m=0}^{M-1} \sum_{n=0}^{N-1} I_{nom}(m, n) I_{exp}(m - k, n - l) \quad , \quad \begin{cases} -(M - 1) \leq k \leq (M - 1) \\ -(N - 1) \leq l \leq (N - 1) \end{cases} \quad (2.11)$$

Here, I_{nom} and I_{exp} are images of size $M \times N$. Let the mean of the auto-correlation matrix be \bar{C} , and the maximum be \hat{C} . An image which closely matches the nominal case it is compared to will exhibit a relatively low mean autocorrelation value indicating a narrow distribution. Additionally, the maximum auto-correlation value will be higher than a case where the experimental image is very different from the nominal image it is compared to. Given these facts, a metric for determining the location of a loose bolt could be developed, $\bar{\bar{C}}$, defined by:

$$\bar{\bar{C}} = \frac{\hat{C}}{\bar{C}} \quad (2.12)$$

Inclusion of both the mean and maximum auto-correlation values in this metric yields a more sensitive parameter than relying on one value alone. The image cross correlation technique was tested in a case study involving a single loose bolt (B5 in Fig. 2.3). Bolt 5 was loosened by 50% relative to the other bolts in the panel, and sparse array data was collected. Figure 2.8 shows the resultant experimental TFM image and the corresponding nominal image generated for bolt 5 with a 70

excitation pulse. In these images, the white diamond represents the location of the loose bolt. Cross-correlation was performed for the experimental image and all 20 nominal images, and the resulting correlation metric distribution is shown in Fig. 2.9. As expected, there is a peak correlation value corresponding to bolt 5, the actual loose bolt. Despite this, there are several bolts with very similar correlation values which is not desirable. It was observed that there is significantly more noise in the experimental image, and the damage presents itself outside of the ellipse shaped panel rather than at the loose bolt itself. The latter problem could likely be attributed to an inaccurate group velocity approximation. In order to improve the correlation metric distribution, these problems are addressed in the following section through the use of group velocity adjustment and image filtering.

2.4.2 Group Velocity Correction and Filtering

To compensate for the inaccuracy in the group velocity approximation, the group velocity of the nominal/theoretical image was varied until a maximum value of \bar{C} was achieved. Particularly, since the experimental image showed damage farther away from the array than the bolt, the group velocity of the nominal images needed to be increased to show a similar damage location outside of the panel. For the bolt 5 loose case, the group velocity of the nominal images was raised from 1.52 km/s to 1.88 km/s to achieve the maximum correlation metric for all bolt number cases and group velocities tested between 1.52 km/s and 2.29 km/s. Additionally, to remove noise from the experimental image, a threshold filter was applied with a

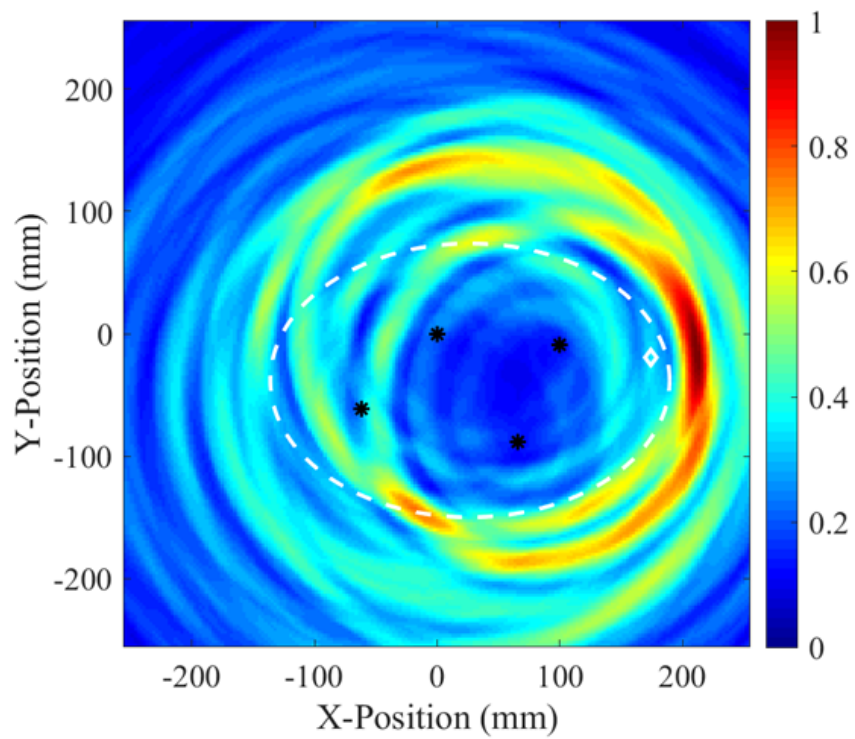
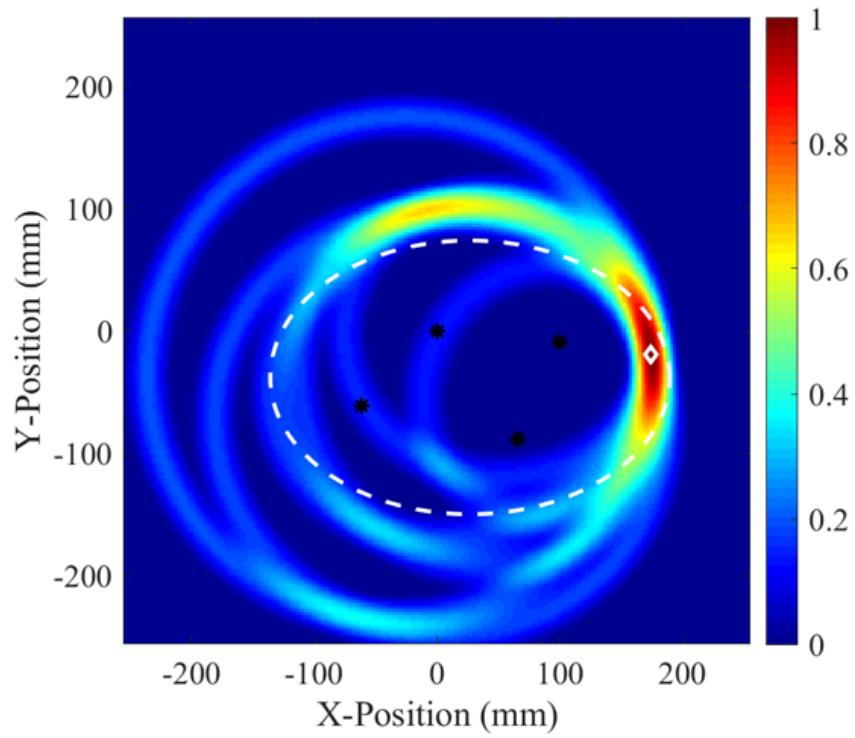


Figure 2.8: Nominal (top) and experimental (bottom) normalized TFM damage images.

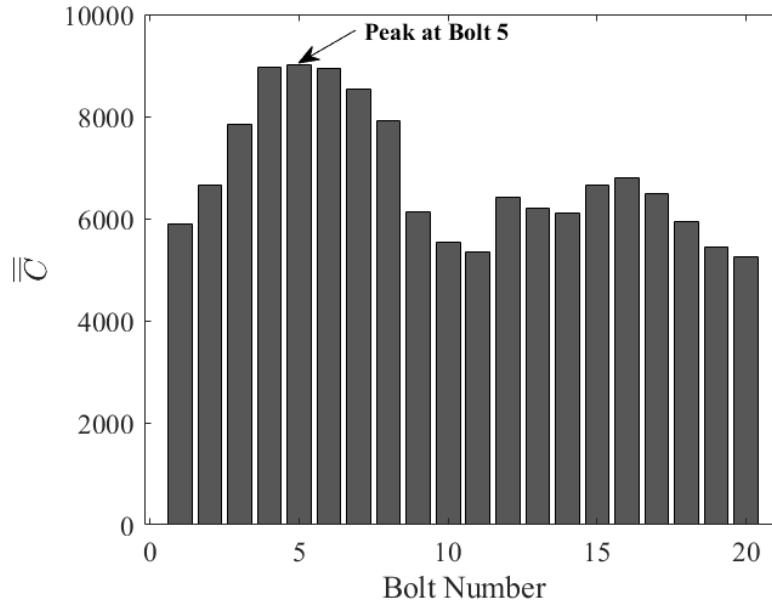


Figure 2.9: Correlation metric, \bar{C} for each bolt number indicating a peak correlation for bolt 5.

cutoff level of 55%. Figure 2.10 shows the resulting group velocity adjusted nominal image and the filtered experimental image. It can be observed that the location of maximum damage is near bolt 5 but outside of the panel for both images with the group velocity correction. The resulting distribution of the correlation metric, \bar{C} for all bolt numbers is shown in Fig. 2.11. Here, bolt 5 has a much clearer maximum than that of Fig. 2.9 indicating that the corrections applied improved the sensitivity of the system in determining the loose bolt. Moreover, the peak value of \bar{C} increased by more than 50% for bolt 5, while the values of \bar{C} decreased for bolts far away from the actual loose bolt.

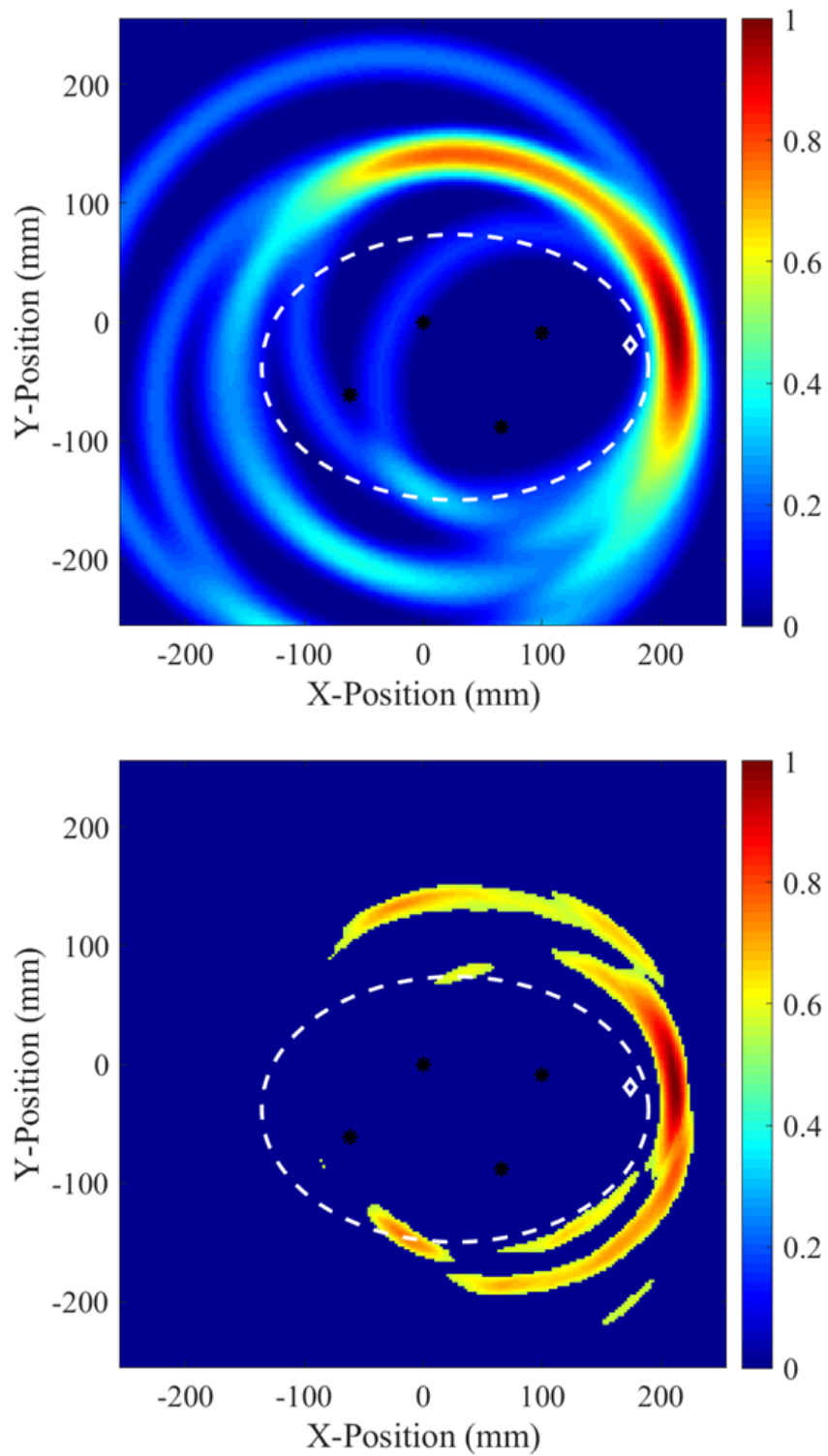


Figure 2.10: Nominal (group velocity adjusted) and experimental (filtered) TFM damage images.

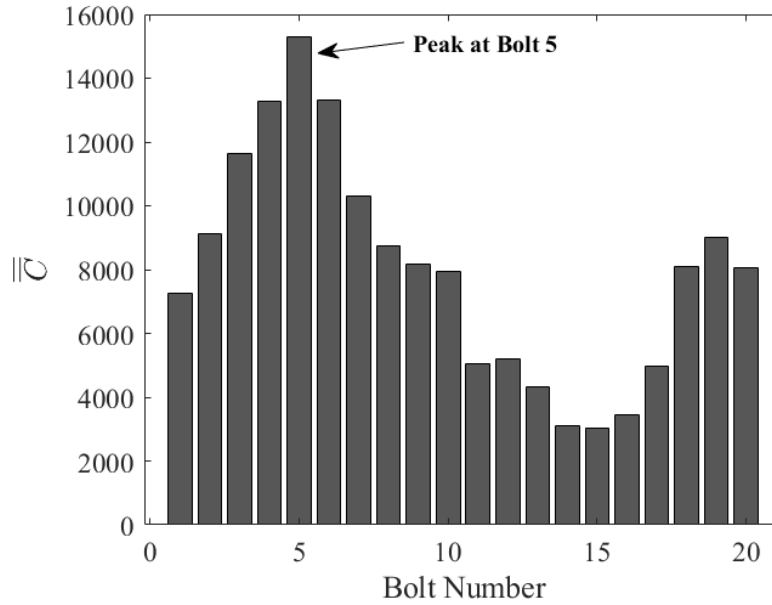


Figure 2.11: Correlation metric, \bar{C} for each bolt number indicating a peak correlation for bolt 5.

2.4.3 Damage Image Maxima Method

A final autonomous damage characterization algorithm was studied which simply measures the locations of the maximum damage levels in the nominal and experimental TFM damage images. This parameter which will be defined as d_{max} gives the distance between the maxima of the nominal and experimental images as in Eq. 2.13.

$$d_{max} = \sqrt{(x_{exp} - x_{nom})^2 + (y_{exp} - y_{nom})^2} \quad (2.13)$$

Applying the same example of the bolt 5 loose case yields the relationship shown by fig. 2.12. There is a distinct minimum value of d_{max} corresponding to bolt 5 indicating that the bolt 5 nominal image has a maximum that is closest to the location of the maximum in the experimental image. This approach is significantly

simpler computationally than image cross correlation, and group velocity adjustment is not required to achieve the result presented. This provides another option for an algorithm to distinguish if a bolt is loose, but this approach would determine the loose bolt by searching for the minimum value as opposed to the maximum with the correlation algorithm.

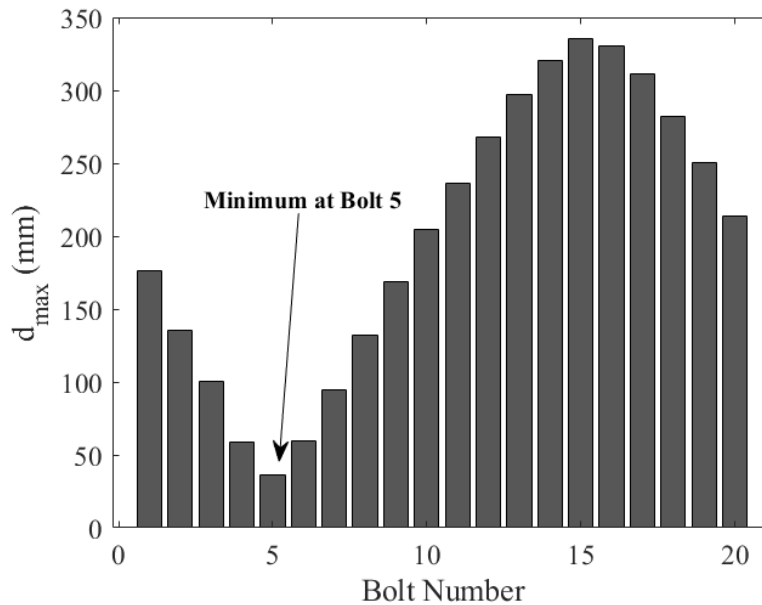


Figure 2.12: Maxima comparison metric, d_{max} for each bolt number indicating highest correlation (minimum distance between maxima) for bolt 5

2.4.4 Discussion

Despite the apparent ability for these autonomous methods to produce the intended result of correctly choosing a loose bolt, practically this may not be very useful. It is unlikely that only exactly one bolt would be loose, and the methods shown do not establish a threshold alert level. This alert level could be established experimentally or through use of a damage index algorithm [30], but a large amount

of data would need to be gathered to establish a reliable alert level. Machine learning may provide a solution to this type of problem, but the effort involved may not be justifiable either especially if there are many complex systems on an aircraft which need monitoring. Training a machine learning algorithm would be expensive both computationally and in terms of flight hardware which must be damaged in a realistic manner. Thus, it may be most practical to establish a technician review requirement to inject necessary subjectivity into review of the data. The following section entertains this option by introducing manual review of damage images.

2.5 Manual Technician Review Study

Given the apparent need for manual technician review, an anonymous survey was designed which tested how effectively a user of the presented SHM system could diagnose damage with minimal training. The survey was distributed to undergraduate and graduate engineering students with participation being on a voluntary and anonymous basis. Volunteers had no prior experience with GLW SHM approaches or interpreting the spatial damage images of these techniques, and no data was collected about the participants. All data was collected through an anonymous online form. The 36 volunteers were presented with a set of seven cases shown in Fig. 2.13 in which one bolt on the panel was set to a torque of 3.39 Nm while the others were torqued to 6.78 Nm. Participants were asked to identify the loose bolt based on these TFM and TFM/SCF compounded threshold spatial damage images. Note that in Fig. 2.13 white circles indicate the loose bolt, however these

are only shown for the reader here and were not present on the images shown to volunteers. Additionally, units shown to the survey participants were in inches since these units were likely more familiar to the participants than SI units. Given 36 volunteers and 7 damage cases, a total sample size of 252 was achieved considering each volunteer-case combination as a unique sample in evaluating the SHM system as a whole. Volunteers were presented with a brief set of training instructions and informed that they would act as a maintenance technician who was inspecting the panel to find a loose bolt. This set of instructions included an example explaining suggestions on how to interpret the TFM and combined TFM/SCF images. For the complete contents of the survey, see the supplemental multimedia package.

The results summarized by table 2.1 show that in nearly two thirds of all cases (63.5%), the bolt which was actually loose was picked by the volunteer. 94% of the time, the volunteer picked either the correct bolt or the bolt next to it, and no volunteers picked bolts which were more than 2 bolts away from the actual loose bolt for all cases. Each of these percentages (63.5%, 94%, and 100%) is a significant improvement over the probability of randomly guessing the correct bolt or an adjacent bolt (5%, 15%, and 25% respectively). This shows that for the simple damage cases tested here, with minimal training, users could interpret damage maps fairly accurately. Given these results, in a practical application the ideal maintenance action for a technician would be to check the torque on bolts within a two bolt radius of the bolt that they picked using these spatial damage images. This reduces their workload by a factor of four if the maintainer elects to only inspect these five bolts and not all twenty. With this inspection scheme, a loose bolt would not have been

missed since the correct bolt was picked within a two bolt radius for all 252 samples.

Note that in some cases, the correct bolt was easier to identify than others. For example, in case 5 no volunteers picked the correct bolt, while in case 6 all volunteers picked the correct bolt. Due to the geometry of this particular panel and PZT arrangement, certain areas containing loose bolts were found to be more conducive to producing easy to interpret images. Thus, the system is not accurate enough to guarantee zero missed detections within a one bolt radius or better with human review. Additionally, the survey presented here does not address cases in which multiple bolts are loose. Moreover, practical employment of this system would need to establish a threshold damage level above which technician review is required. This would prevent false alarms through misinterpretation of noise in the baseline subtracted signal. A complete set of instructions may need to include information on the scenario of multiple loose bolts, for example by stating that if the damage image magnitude is above a certain level, but the location of the damage is inconclusive, the technician should inspect the entire panel for loose bolts or damage. Despite the prevalence of these other complex factors which must be considered, this study shows that technicians have the capability to interpret the results of a GLW damage mapping system accurately for simple damage cases in an aircraft structure. For both autonomous damage detection and manual technician review, it is apparent that when designing a GLW damage detection technique, it must be vetted with a realistic complex application, and various factors beyond the basic function of the technique must be considered.

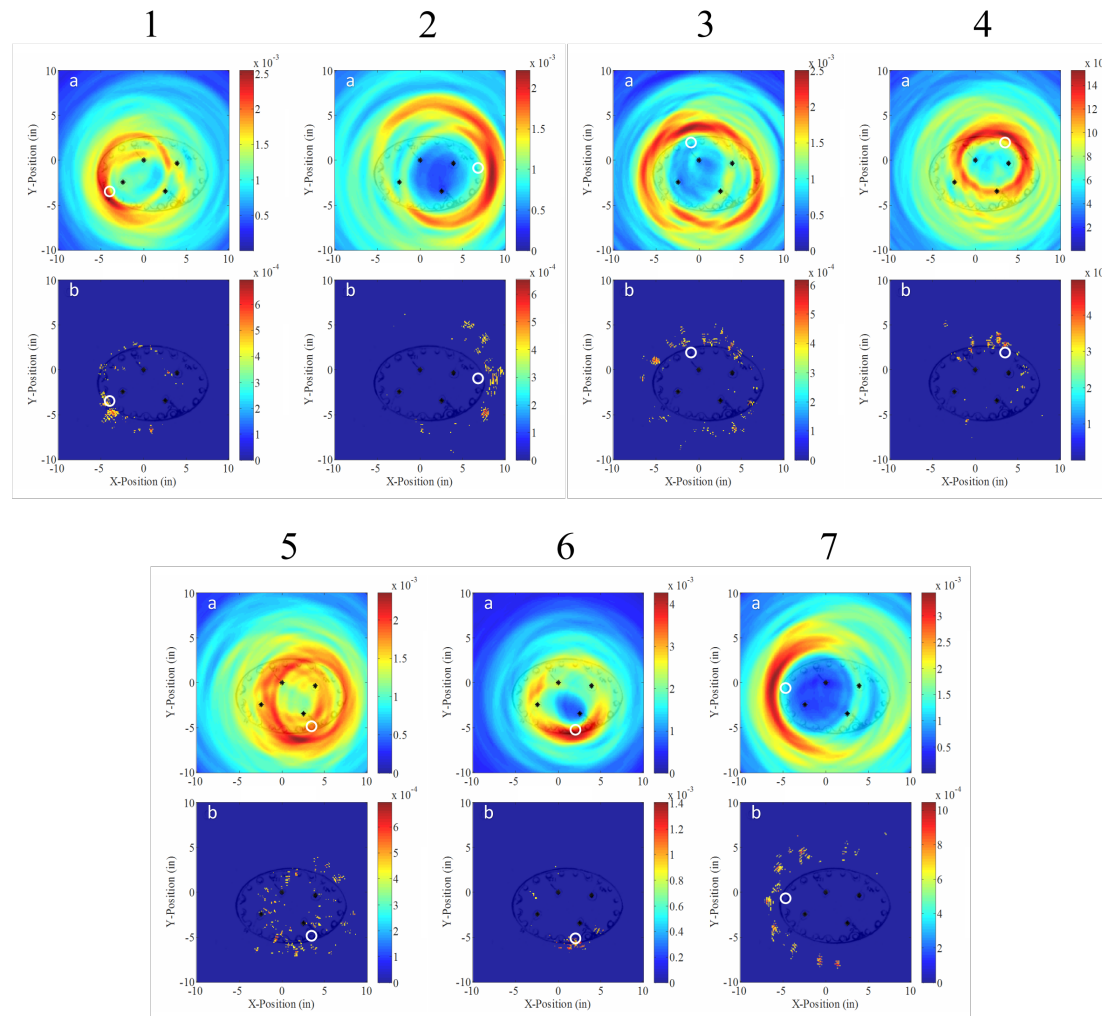


Figure 2.13: Damage cases presented for the blind "technician" survey.

2.6 Chapter Conclusion

In an effort to improve the technical readiness level of SHM for aircraft applications, existing GLW damage localization techniques were applied to a practical case study involving an F/A-18 wing. The goals of this work were to further understand challenges in applying GLW techniques to actual aircraft structures and to study the role of human factors in developing an SHM technique. A sparse piezoelectric array was mounted to a panel on the wing, and a series of damage cases introduced torque loss to fasteners surrounding the panel. GLW pitch-catch signals were recorded for this sparse array, and spatial damage images were generated using TFM and SCF image compounding techniques. Autonomous methods of interpreting these images were explored with success in identifying loose bolts in simple damage cases. A blind study tasked volunteers with interpreting these images in a technician role and showed that with minimal training, participants could reliably interpret damage images to determine the locations of loose bolts within a 2 bolt radius.

Although the presented SHM spatial damage mapping approach is clearly able to produce desirable localization results which a technician could interpret correctly for simple damage cases, it is by no means a total solution. Likely due to the complex and inhomogeneous construction of the wing, damage images were noisier and less clear than studies performed using simple aluminum plates. Additionally, the thick, composite structure of this wing meant GLW signals were relatively weak and noisy. Often techniques are proposed which overlook the reality of realistic

highly complicated structures. Moreover, these sometimes only address a single level of SHM such as Level 1 or Level 2 (Detection or Localization) For practical use, the designer of a new technique should consider the relevance of multiple levels, as one level is often not very useful without another. For example, localization is not meaningful without a means of affirming that damage above some threshold has been detected as was the case with this study. In short, the case study presented in this chapter illustrates the complexity of practical employment of any SHM technique and demonstrates the need for a thorough, holistic approach to developing and analyzing new techniques. GLW techniques likely need to be combined with other types of techniques for a fully functional and redundant system.

Chapter 3: Piper Cherokee Wing Damage Localization

3.1 Introduction

As discussed in Chapter 1, in order to excite and measure Lamb waves in a practical structure, in-situ transducer networks must be installed as part of the system. Use of PZT transducers as the excitation and sensing devices are common due to their simplicity, efficiency, and relatively well-understood properties. Given an excitation voltage and a relatively low excitation frequency, for an isotropic material such as aluminum, a PZT bonded to the surface will excite both the fundamental symmetric (S0) and antisymmetric (A0) Lamb wave modes. However, for many GLW localization algorithms, a structural response consisting of one mode is ideal and greatly simplifies signal processing. One solution to this is to bond collocated transducers on either side of a plate in order to selectively excite or decompose a mode of interest [31]. But it is difficult to collocate transducers accurately, and this practice is impractical for aerospace applications where sensors disrupting an aircraft's outer mold line are not practical for field use. One could also take advantage of the PZT tuning curve to excite the guided waves at frequencies where one mode is dominant, but this cannot perfectly generate only one mode, and it limits the excitation frequencies which can be used significantly [32,33]. As an alternative

to collocated PZTs, a dual PZT transducer SHM concept was developed [34, 35]. These transducers are constructed from a pair of concentric ring and disc PZT-5A elements and thus can be mounted on one side of a plate and allow for highlighting of the constitutive A0 and S0 modes in a GLW signal.

Sparse array GLW methods makes use of a large, spatially distributed network of transducers which ideal for monitoring a large surface area, such as the skin of an aircraft [36, 37]. These methods usually requires a baseline or pristine condition dataset. Baseline-free methods have been developed due to the drawbacks of relying on a baseline such as varying temperature environments and other unknown operating conditions [38, 39]. However, due to the complexity of as-built aircraft structures, methods employing a baseline provide the best localization capability if environmental influences can be controlled or compensated for [40]. Lamb wave theory depends on infinite flat plates, so the introduction of structural features such as stringers, ribs, and rivets creates significant challenges. Riveted structures and plate edges cause a GLW scattering effect, and reflections from plate edges and other features make GLW signals in these structures complex [41–43]. Understanding these features and overcoming the challenges they pose is critical for optimal damage localization.

In this chapter, a sparse array was constructed using dual PZT transducers and was installed on a section of a Piper Cherokee skin plate. Damage to this structure was simulated with magnets in various cases to study the localization capability of the dual PZT array. The GLW signal S0 and A0 modes were highlighted using the dual PZT mode decomposition process, and signals were compared to

a baseline set of data. Sparse array imaging techniques were employed, and the damage localization results are presented and analyzed. Finally, a discussion on the influence of mode decomposition and complex structural features is presented.

3.2 Methodology

3.2.1 Dual PZTs and Mode Decomposition

The basis for using dual element PZT transducers for GLW SHM applications is rooted in the tuning curves of PZT wafers. In other words, the amplitudes of A0 and S0 modes are dependent on PZT wafer size. Manipulation of this property allows for Lamb wave mode decomposition without requiring collocated sensors on two sides of a plate. For this work an array of five dual PZTs was constructed. The placement of this array is explained in further detail in the experimental setup section. In order to decompose the fundamental Lamb wave A0 and S0 modes for a given transducer pair and excitation frequency, two types of pitch-catch signals are needed. For the first signal, $RD_{ij}(t)$, the ring portion of the i^{th} transducer is excited with a 4.5 cycle Hanning windowed toneburst and the inner disc section of the j^{th} transducer measures the GLW response. The other signal, $DD_{ij}(t)$, is formed when the inner disc portion of the i^{th} transducer is excited and the inner disc section of the j^{th} transducer measures the GLW response. Figure 3.1 shows the dimensions of the PZT-5A transducers used for this work as well as a diagram illustrating the signal nomenclature.

For this work, only the two signals presented above were necessary for ade-

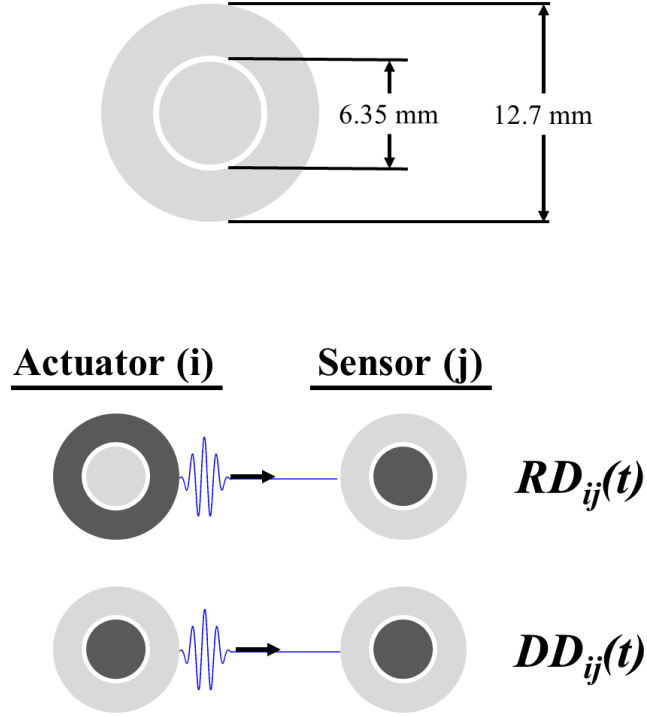


Figure 3.1: Dual PZT dimensions and signal nomenclature (active PZT elements are darkened)

quate highlighting of the constitutive modes, unlike the original baseline free method developed in [35] which uses the full nine available signal permutations. In our case, the sensing PZT is used as if it were a single element transducer similar to [44], i.e., only the central disk is used to measure the structural response for each transducer pair. In order to decompose the individual A0 and S0 modes, the ring and disc signals were combined and scaled according to equations (3.1) and (3.2).

$$A0_{ij}(t) = RD_{ij}(t) - S_{c,ij}DD_{ij}(t) \quad (3.1)$$

$$S0_{ij}(t) = RD_{ij}(t) - A_{c,ij}DD_{ij}(t) \quad (3.2)$$

3.2.1.1 Empirical Scaling Factor Determination

For this work, the scaling factors $A_{c,ij}$ and $S_{c,ij}$ were determined experimentally by comparing the magnitudes of particular modes in the ring and disc signals. For example, the scaling factor $S_{c,ij}$ was determined by measuring the ratio of the amplitudes of the S0 mode first arrivals for $RD_{ij}(t)$ and $DD_{ij}(t)$. Thus, applying Eq. 3.1 with this scaling factor essentially removes the S0 mode from the initial signal, and the opposite is true applying Eq. 3.2. It should be noted that the $A_{c,ij}$ scaling factors were difficult to determine in many cases due to the fact that S0 reflections often overlapped with the A0 direct wave causing difficulties in estimating the amplitude of this mode. For this reason, $A_{c,ij}$ values are rough approximations and not as precise as the $S_{c,ij}$ values. Despite this, the scaling factors were accurate enough to decouple the A0 and S0 modes substantially. The experimentally measured scaling factors are shown in Tables 3.1 and 3.2 for various excitation frequencies and the ten unique sensor-actuator combinations. Although the five transducers were nominally identical in shape and size, scaling factors varied significantly between pairs, possibly due to slight differences in construction and installation. Thus, to be as precise as possible, the scaling factors were measured for each transducer pair.

The Dual PZT mode decomposition technique was verified using a pair of transducers mounted on a Piper Cherokee wing. This experimental setup is explained in significant detail in subsequent sections. The verification of the decomposition process is shown in Fig. 3.2 and Fig. 3.3. Here the signal, $DD_{ij}(t)$, is used as the reference A0 and S0 coupled signal since it is essentially equivalent to a signal

that would be found using more common single element PZT discs. Figure 3.3 shows that the dual PZT processing method is at a minimum able to highlight the first arrival and edge reflections of a particular mode. This technique also substantially increases the amplitude of each decoupled signal.

Table 3.1: Ratios of S0 amplitudes between RD_{ij} and DD_{ij} , $S_{c,ij}$

Frequency, kHz	Actuator (i) - Sensor (j) Pair Numbers									
	$S_{c,12}$	$S_{c,13}$	$S_{c,14}$	$S_{c,15}$	$S_{c,23}$	$S_{c,24}$	$S_{c,25}$	$S_{c,34}$	$S_{c,35}$	$S_{c,45}$
80	1.238	1.195	1.269	1.338	1.694	1.667	1.910	1.910	1.819	1.742
100	1.294	1.232	1.323	1.458	1.648	1.493	1.775	1.775	1.590	1.622
120	1.349	1.319	1.412	1.467	1.596	1.498	1.695	1.695	1.596	1.555
140	1.396	1.279	1.390	1.491	1.508	1.480	1.702	1.702	1.556	1.433
160	1.352	1.383	1.414	1.442	1.459	1.341	1.409	1.526	1.526	1.558

Table 3.2: Ratios of A0 amplitudes between RD_{ij} and DD_{ij} , $A_{c,ij}$

Frequency, kHz	Actuator (i) - Sensor (j) Pair Numbers									
	$A_{c,12}$	$A_{c,13}$	$A_{c,14}$	$A_{c,15}$	$A_{c,23}$	$A_{c,24}$	$A_{c,25}$	$A_{c,34}$	$A_{c,35}$	$A_{c,45}$
80	-1.122	-1.164	-1.143	-1.000	-1.030	-1.072	-1.147	-1.000	-1.177	-1.000
100	-1.839	-1.413	-1.309	-1.177	-1.693	-1.534	-1.618	-1.621	-1.663	-1.066
120	-2.379	-1.531	-1.688	-1.205	-2.468	-2.872	-2.412	-2.051	-2.009	-1.331
140	-2.286	-1.934	-1.901	-1.179	-3.240	-2.860	-3.466	-2.323	-2.472	-1.622
160	-1.973	-2.018	-1.896	-1.541	-3.715	-2.835	-3.687	-2.563	-2.268	-1.957

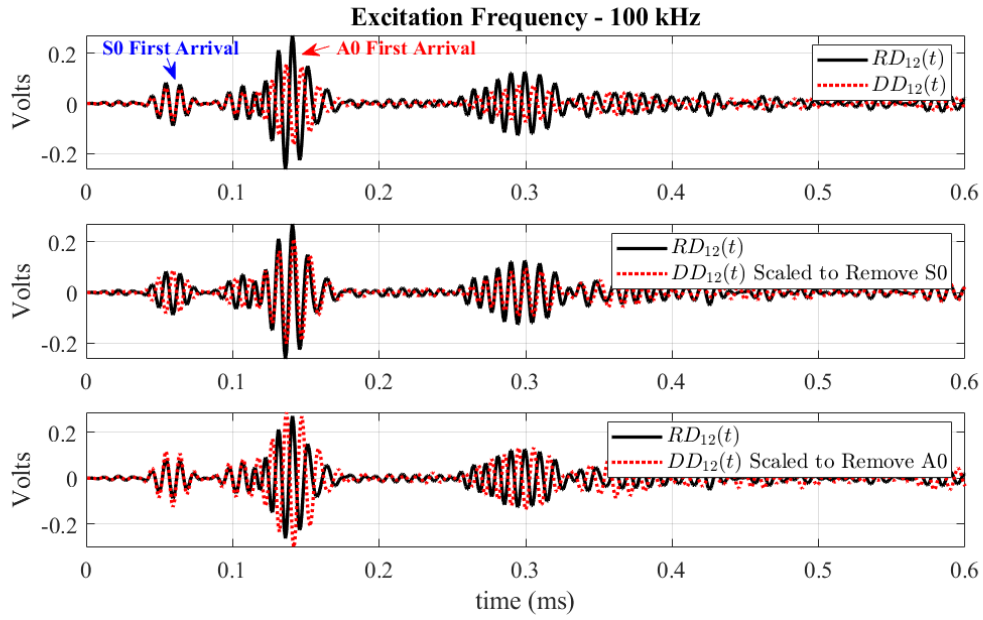


Figure 3.2: Signal scaling process for mode decomposition

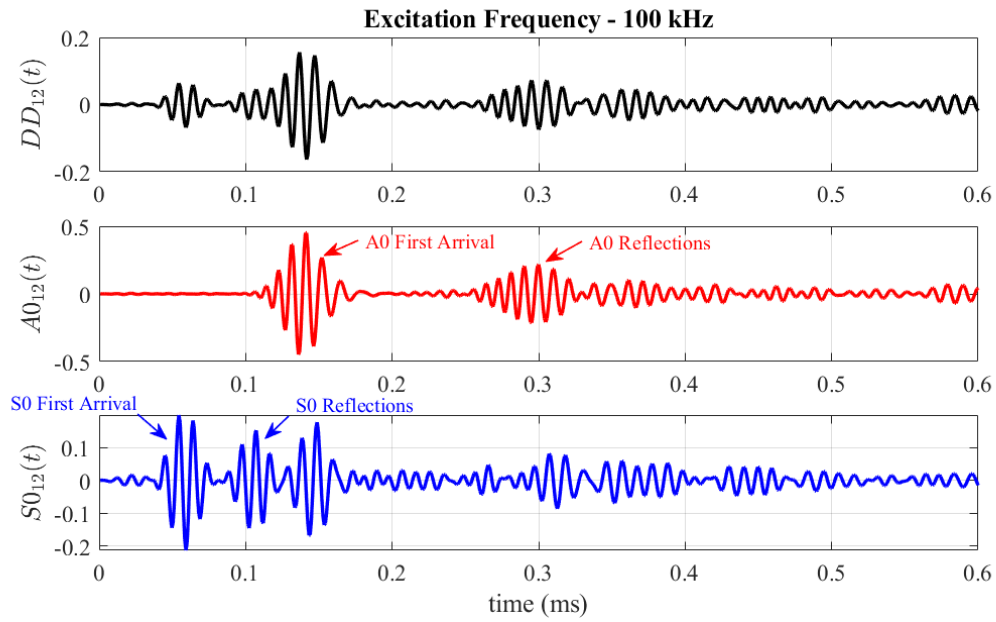


Figure 3.3: Demonstration of signal decomposition

3.2.2 Sparse Array Technique

With the Dual PZT mode decomposition method verified, it could now be applied using the sparse array technique to evaluate its efficacy in damage localization on a wing. As described in chapter 2, the sparse array technique involves a network of spatially distributed transducers which are used to inspect a large area for damage. For this chapter however, dual PZTs will make up this transducer network. Baseline subtraction was used again to highlight the scattered portions of the signal from any damage introduced after the baseline was taken. These portions of the signal were then converted from the time domain to the space domain using the group velocity of a particular mode through a time of flight calculation given by Eq. 2.3.

The signal must be assumed to predominantly consist of only one mode for this conversion to be successful. In our case, the decomposed signals were used providing a potentially more accurate result. For a given point (x, y) in the inspection area and a sensor actuator pair (i, j) , the instantaneous signal amplitude, a_{ij} of the baseline subtracted signal of interest at the corresponding time from Eq. 2.3, t_{ij} was assigned to the damage image matrix $I_{ij}(f, x, y)$. The instantaneous signal amplitude was determined from the signal of interest $s_{ij}(t)$ using a Hilbert transform as described by Eq. 2.2 in chapter 2.

This space domain conversion is repeated for all points in the desired inspection area filling the image matrix I_{ij} for a sensor-actuator pair (i, j) . This is repeated for all sensor-actuator pairs, and each image is combined yielding a triangulation

effect at points of possible damage through intersecting ellipses. For this chapter, two triangulation methods were used: summation and correlation algorithms. These algorithms are described in more detail by [16, 45], but the image forming equations are given below.

$$I_{sum}(f, x, y) = \sum_{i=1}^N \sum_{i=1}^N I_{ij}(f, x, y) \quad i \neq j \quad (3.3)$$

$$I_{corr}(f, x, y) = \prod_{i=1}^N \prod_{j=1}^N I_{ij}(f, x, y) \quad i \neq j \quad (3.4)$$

The correlation algorithm provides greater clarity by focusing more on ellipse intersections; however, it can be prone to false alarms and missed detections if incidental intersections outweigh the intersection at an actual damage location or if there are multiple damage locations present in the inspection area. A higher number of transducers tends to produce a better result for both methods, but there must be a trade-off in order to limit weight, cost, and excessive data acquisition requirements. For the localization algorithms, the experimentally determined group velocities shown in Fig. 3.4 were used. For the frequency range of interest (40-200 kHz), a PZT bonded to a 1mm aluminum plate will excite only the A0 and S0 modes since this range is below the cutoff frequencies for higher order modes.

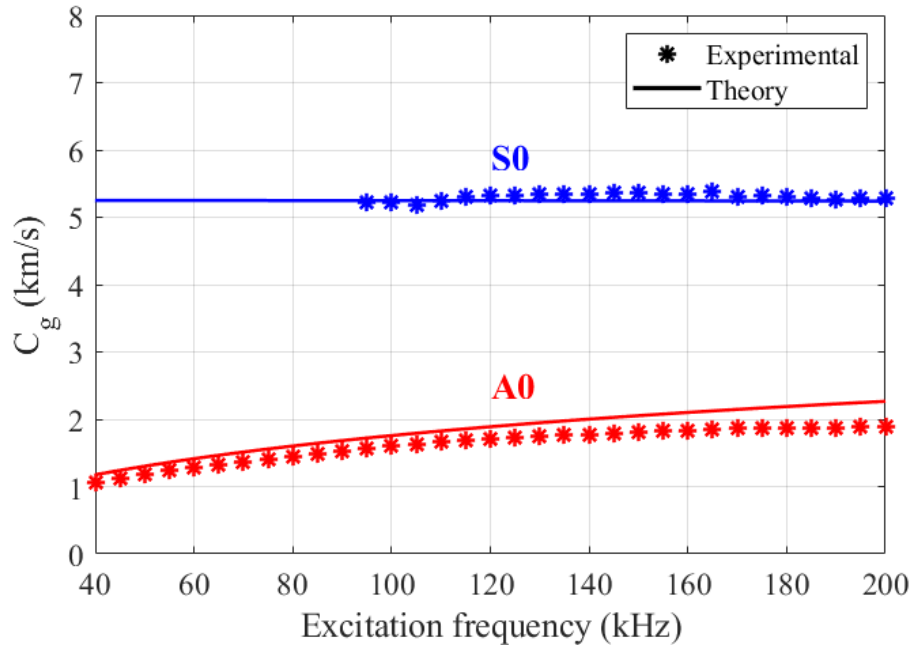


Figure 3.4: Experimentally determined group velocities and theoretical values assuming typical material properties for a 1mm thick Al2024 plate.

3.2.3 Experimental Setup

3.2.3.1 Piper Cherokee Wing

Experimental work for this study used a Piper Cherokee wing section shown in Fig. 3.5 as the test specimen. The panel of interest was constructed from a 1-mm thick aluminum alloy skin plate and was built up with various stringers, ribs, and a spar. These features were generally riveted to the skin plate, and no other bonding materials were used. The only modification to this structure was a strand of tacky tap on the sharp edge where the specimen was cut. This was placed so that strong reflections from this unrealistic edge would be reduced. The five-element transducer array was constructed in the shape of a spiral as a non-axisymmetric distribution was desired for optimal performance. Figure 3.6 details the design of this spiral

array which was formed using concentric, rotated pentagons. Five transducers were used to balance the damage localization quality and undesirable traits as discussed in the previous section. The array was positioned on the bottom of the wing just aft of the leading edge as shown by Fig. 3.7. The array was placed on a section of skin bordered by ribs and stringers such that none of these features were contained within the array with several inches of offset on all sides. This was done so that the influence of each structural feature could be assessed individually through various damage cases. It should be noted that for an array inspecting the entire area shown in Fig 3.7, a wider distribution of transducers could provide better imaging results, but for this work the influence of the complex structural features was of interest.

3.2.3.2 Magnet Damage Simulation

Damage was simulated to the wing skin using a strong pair of magnets placed on either side of the skin. Use of magnets as opposed to real damage was preferred so that several damage locations could be investigated without permanently changing the baseline structure. When the magnet pair pinches the skin, it generates a localized force which produces GLW scattering similar to an actual crack. A separate study verified that this assumption is valid and that use of a magnet provides a more conservative means of simulating damage because its scattering effect is weaker than that of a crack. For this study, a 610x610x1mm Al6061 plate with two 6.35mm diameter single element PZT discs (shown in Fig. 3.8) was used to compare the GLW responses with a crack and magnet pair. Single element transducers were

sufficient for this evaluation since PZT size and shape are not important when considering the difference in strength of reflections between a crack and magnet pair. The qualitative difference in reflection strength will be the same regardless of the transducer types used. The crack and magnet pair were each 20 mm in length and placed in the same location and orientation on the plate. Results of this study are presented in the results and discussion section.

3.2.3.3 Data Acquisition

For this work, 4.5 cycle Hanning windowed tonebursts were used as excitation since this provides ideal dispersion characteristics and creates a symmetric waveform which makes visual interpretation of peak amplitude and dispersion simpler. Excitation frequencies between 40 and 200 kHz were used with a peak to peak amplitude of 160 V. GLW signals were amplified by a signal conditioning unit and were recorded at 1.25 MHz using a NI DAQ. All signals were filtered using a 4 pole 35kHz-350kHz bandpass Butterworth filter, and an ensemble average with $n = 100$ further removed noise from the signals. Efforts were made to reduce electromagnetic interference (EMI) or excitation crosstalk as much as possible, but this signature was still present in many of the signals.

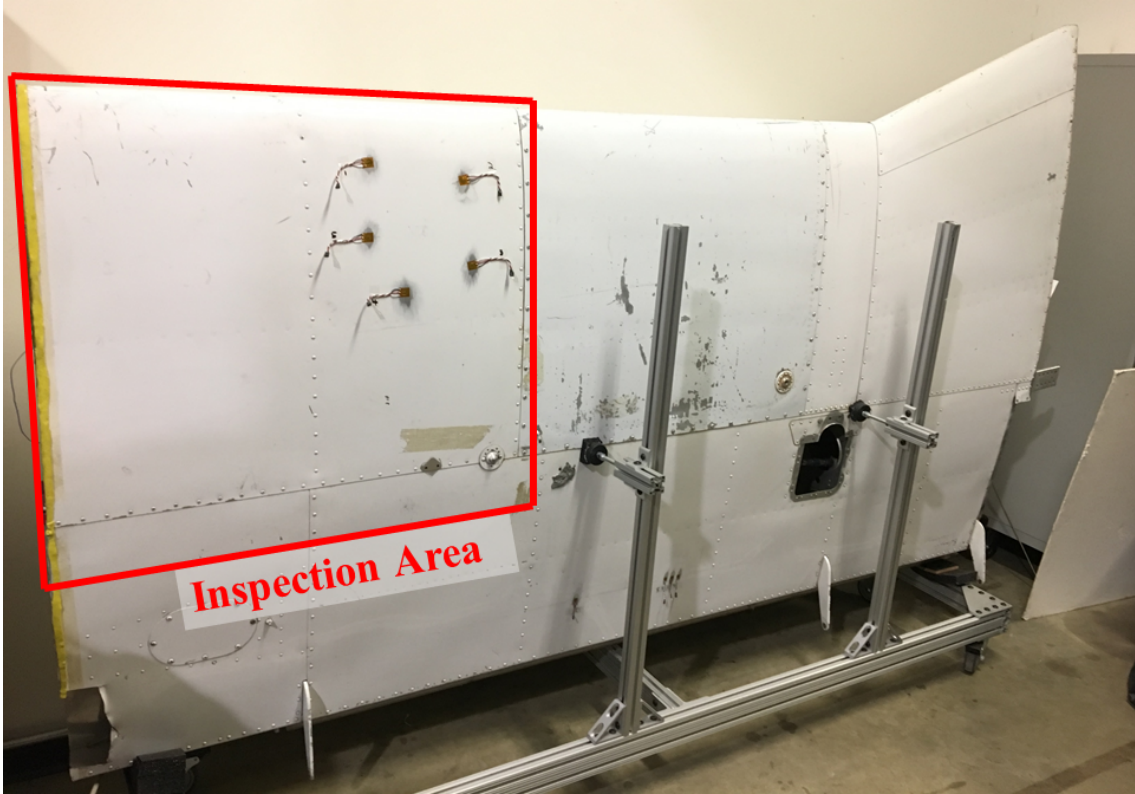


Figure 3.5: Bottom of Piper Cherokee Wing

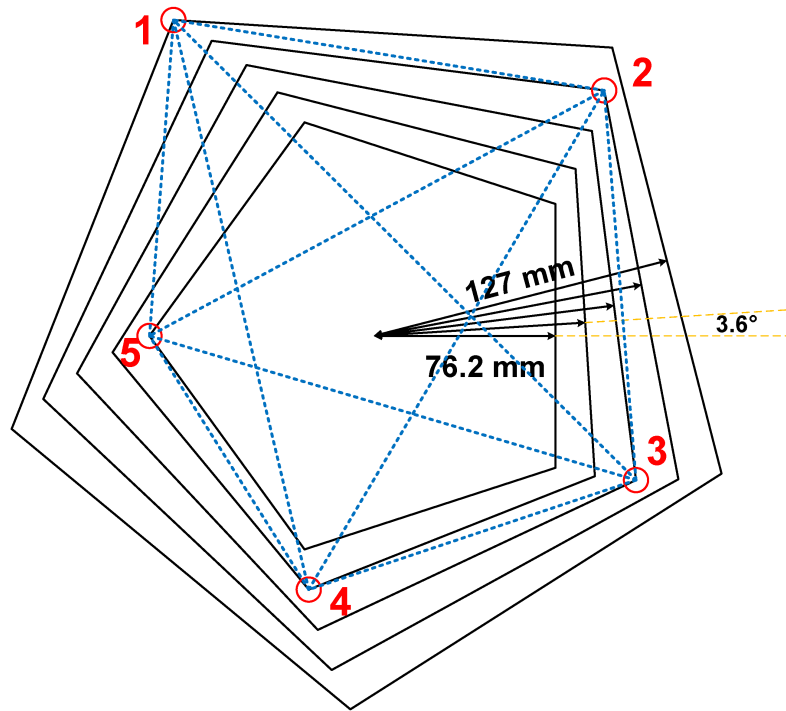


Figure 3.6: Design of the sparse array

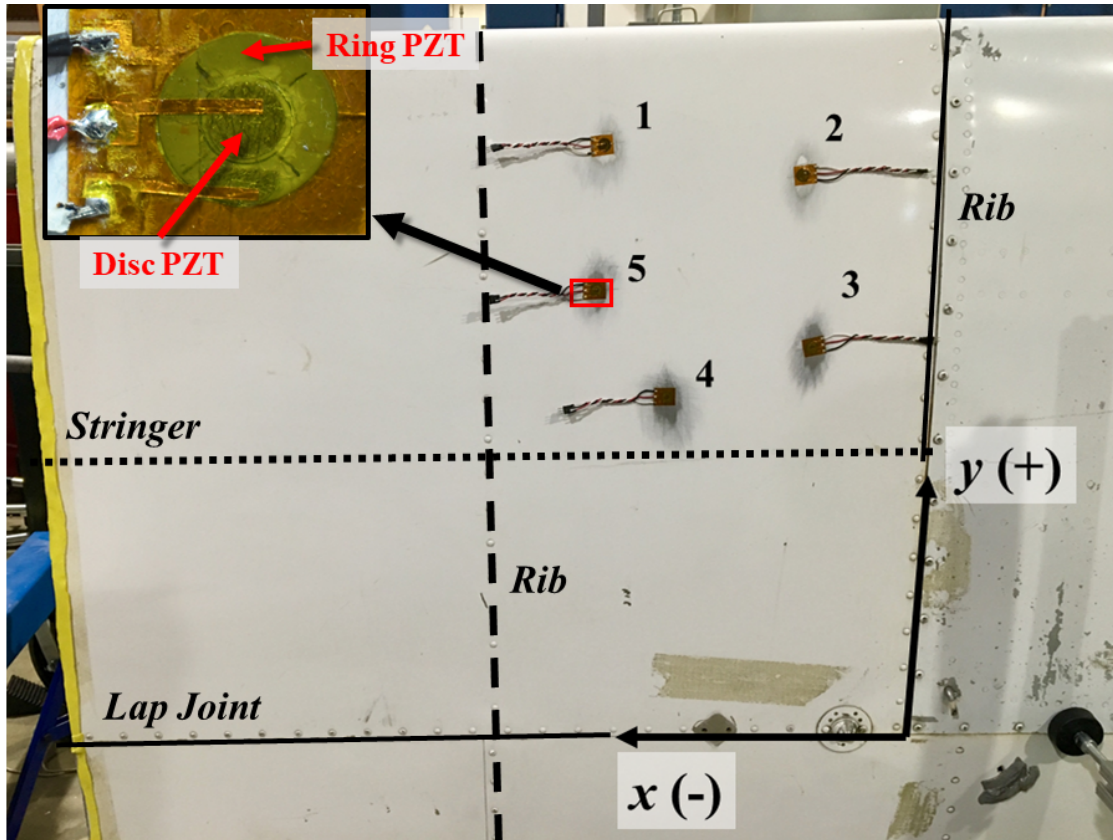


Figure 3.7: Sparse PZT array using dual PZT transducers and details of damage inspection area

3.3 Results and Discussion

A series of studies assessed the capabilities and limitations of the mode decomposition technique combined with the sparse array method. Five case studies are presented here, each testing different aspects to the present method including range, individual mode effectiveness, and the influence of complex structural features such as ribs, stringers, and lap joints. First, the results of the magnet and crack damage comparison are presented.

3.3.1 Magnet Damage Simulation Validation

To compare the strength of GLW scattering between a pair of magnets and a crack in the plate, we define a nondimensional signal amplitude, \bar{A} :

$$\bar{A} = \frac{\max\left(\left|s_{dam}(t) - s_{BL}(t)\right| + i\mathcal{H}\left(s_{dam}(t) - s_{BL}(t)\right)\right)}{\max\left(\left|s_{BL}(t) + i\mathcal{H}\left(s_{BL}(t)\right)\right|\right)} \quad (3.5)$$

Here the peak baseline subtracted damage signal envelope, is normalized by the peak amplitude of the baseline signal envelope. The envelope is approximated using a Hilbert transform. Figure 3.9 shows this nondimensional amplitude ratio for the magnet pair and crack damage cases at various excitation frequencies. As discussed further in the experimental setup section, single element transducers were sufficient for this study, and the results could be applied to the dual PZT transducers used for the Piper wing case studies. This is because this study is comparing the relative strength of scattering due to a crack and magnet pair, and the transducer is not the item of interest. The results of this magnet study indicate that reflections from the crack are roughly 2 to 3 times as strong as those from the magnet pair used to simulate damage. This shows that use of the magnet pair will certainly provide a means of simulating a crack, but that it will provide conservative results due to the weaker scattering effect. For example, this implies that an actual crack may be detectable at a farther distance from the array than is found with the magnet pair. GLW time domain plots were also compared for each damage type as shown by Fig. 3.10. The baseline subtracted signals for the magnet pair and crack were

mostly similar with differing amplitudes and slight phase shifts in some cases, but the peak amplitudes of the reflection packets were in nearly identical time locations. This confirms similar scatter signal composition for the crack and magnet but with differing amplitudes. In general, the magnet pair was shown to be a conservative means of simulating damage to the aircraft skin. With this verified, the results of the five wing damage case studies are presented in the following sections.

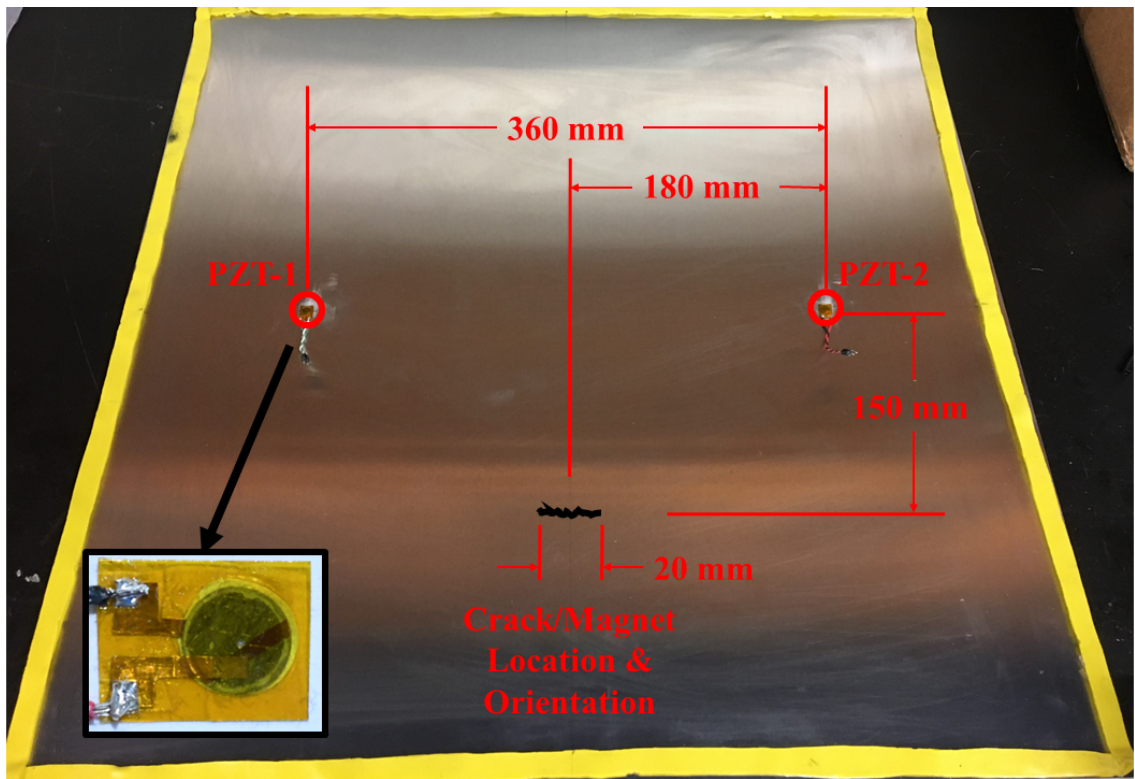


Figure 3.8: Plate and transducers used for magnet damage simulation study.

3.3.2 Wing Case Study 1 - Basic Damage Assessment

In the first simulated damage case, a magnet pair was placed approximately 0.25 m from the center of the array (down and to the left). This case represented one of the simplest location for damage detection since no structural features lie

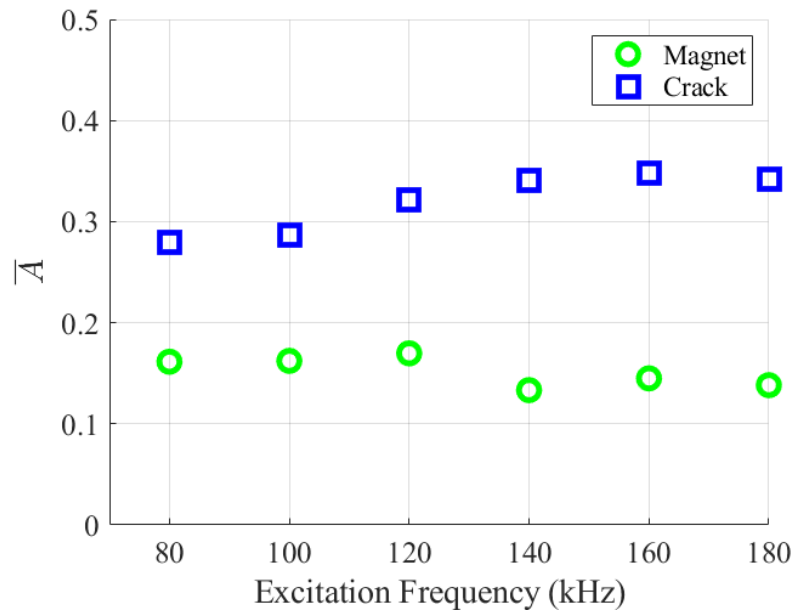


Figure 3.9: Nondimensional signal amplitude, \bar{A} for a magnet pair and crack

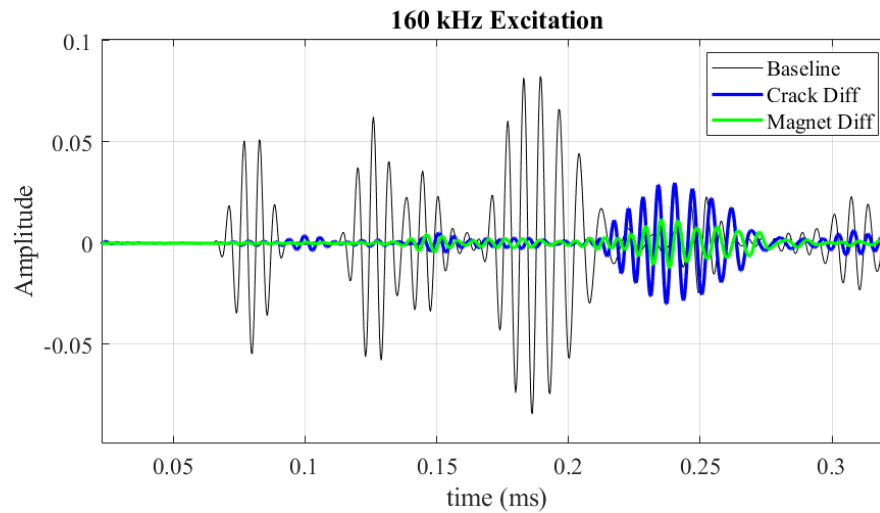


Figure 3.10: Comparison of baseline subtracted signals for a magnet and crack

between the array and the damage, and the close proximity limits attenuation of any scattering due to damage. Thus, this was an ideal starting point to check the function of the mode decomposition and sparse array combined method. Figure 3.11 shows the results for this case using the A0 and S0 decomposed modes with the image summation and correlation algorithms. For the A0 signal images, the A0 group velocities were used. Similarly, S0 signal images employed the S0 group velocities. The excitation frequency shown in the figure is 140 kHz, and similar results were obtained for the frequencies sampled between 80 and 160 kHz. Each image shows structural features such as ribs and stringers as dashed lines as well as the dual PZT array with each transducer represented by the symbol x. The location of the clamped magnet pair is represented by a white star. For the summation images (left), the A0 decomposed mode (top) yielded a clearer and more accurate damage map, although the damage was also visible on the S0 mode damage map. The correlation algorithm images (right) were generally clearer than the summation algorithm images due to its stronger weighting of ellipse intersections. For the correlation algorithm image, the A0 mode decomposed signal was also more accurate and precise than the S0 mode decomposed signal. The S0 mode signal also produced more spurious artifacts in the image away from the actual damage location. However, all methods clearly showed the presence of damage relatively accurately for this simple case demonstrating the basic functionality of the presented method.

3.3.3 Wing Case Study 2 - Damage Far from the Array

The next study examined the range of damage detection and potential influences of a rib mounted to the skin plate by placing simulated damage over 0.5 m from the center of the sparse array with a rib joint in the direct path to the damage. Due to the dispersive nature of the A0 mode and the relatively long distance of the damage from the array, this mode did not accurately locate damage as its reflections were likely too weak. Thus, only the decomposed S0 mode summation and correlation images are shown in Figure 3.12. Both algorithms show damage at the appropriate location using the experimentally determined S0 mode group velocity with an excitation frequency of 140 kHz. Again, similar results were obtained between 80 and 160 kHz. This figure also highlights the difference between the two algorithms for a single damage location case. Henceforth, only the correlation algorithm images are shown since the summation algorithm images are typically similar but less clear. In general, this study demonstrates the advantage of using the S0 mode for maximum inspection range, and it shows that using the decomposed signal, reflections from damage are not attenuated beyond detection at over 0.5 m from the array with a rib in the propagation path.

3.3.4 Wing Case Study 3 - Damage within the Array

For the third case study, damage was placed near the center of the array, as this could pose potential problems with first arrival packet interference. Additionally, the close proximity of damage to the array implied that both the S0 and A0

reflections would be relatively strong, and an assumption that the signal would be predominantly one mode may not provide ideal results in all excitation frequency cases. Figure 3.13 demonstrates this by comparing the damage images for the undecomposed and decomposed S0 mode signals using the S0 mode group velocity with a 140 kHz excitation. Similar images were generated for the excitation frequencies examined between 80 and 160 kHz. On the left side of the figure, it is evident that the undecomposed signal had dominant A0 mode reflections, so use of the faster S0 mode group velocity provided a false alarm at an inaccurate damage location while showing no damage at the actual damage location. Use of the A0 group velocity would have been more appropriate, but without *a priori* knowledge of the damage location it would be difficult in practice to know which group velocity to use for the undecomposed signal. By using the decomposed S0 signal, the spurious A0 mode reflections are clearly removed, and use of the S0 group velocity yields a damage image that accurately locates damage. This case study demonstrates that the decomposed S0 mode signal can be used for damage detection close to the array where A0 reflections are typically dominant. Mode decomposition removes these reflections allowing the S0 group velocity to be used to provide an accurate image. This case suggests a new opportunity to use only the S0 mode to search for damage both close to the array and far from it without a need for excitation tuning. This reduces the uncertainty which would exist from using both modes to search for damage in near and far scans of the specimen. Use of one mode for all examination of the specimen significantly simplifies practical employment of the sparse array method.

3.3.5 Wing Case Study 4 - Damage Across the Leading Edge

The fourth case study evaluated potential difficulties that might be introduced by the sharply curved section of skin at the wing's leading edge. The magnet pair was placed roughly in line with the center of the array horizontally and just less than 0.5 m away from the array in the y direction. Note that since the plate is curved along the leading edge of the wing, the y direction represents the arc length perpendicular to the x direction. This distance was measured with a string to ensure proper measurement of the magnet's location along the curved surface. This placement put the magnet pair on the top of the wing with the sparse array on the bottom. However, the magnet was in the same continuous section of skin plate as the sparse array. Figure 3.14 shows that for the most part both the S0 decomposed signal and the A0 decomposed signal were successful at localizing the damage using the S0 and A0 group velocities respectively. The S0 mode decomposed signal provided a more significantly accurate and precise localization, and the results were similar for all excitation frequencies studied between 80 and 160 kHz. It would be reasonable to assume that the leading edge curvature did not significantly influence the GLW propagation since localization was accurate for the S0 decomposed signal. It should also be noted that the strength of the scattering due to the magnet was relatively strong since there were no stringers or ribs in the direct path of the GLW propagation. Since the damage was a similar distance from the array as case 2, these results indicated that the rib in the propagation path of case 2 likely reduced the scattered wave's strength since it exhibited weaker reflections. This is likely

due to the riveted interface between the plate and rib, and a joint with an adhesive material would likely exhibit even greater attenuation. Despite the stronger signal strength in case 4, the dispersion of the A0 mode likely reduced the effectiveness of the A0 decomposed damage image.

3.3.6 Wing Case Study 5 - Damage Across a Lap Joint

The final case study examined the influence of a lap joint on damage detection capabilities. This lap joint connects two skin plate sections with rivets, and this sharp discontinuity was expected to reduce the amplitude of GLW reflections due to damage across the joint. To study this, simulated damage was placed just below the lap joint on a separate plate section from the array. Due to the distance from the array, the A0 mode decomposed signal was not effective in locating this damage, so Fig. 3.15 looks at the S0 mode only. Particularly, Fig. 3.15 compares the effect of signal decomposition on damage image effectiveness with a 140 kHz excitation. Without mode decomposition, the S0 mode reflections due to introduced damage are not high enough above noise to locate this damage correctly, and a false alarm is generated in an inaccurate location. With mode decomposition, the image correctly shows damage at the damage location with a few spurious reflections. This case study suggests that the decomposed S0 mode signal can increase the damage detection sensitivity, and that mode decomposition makes damage detection across lap joints possible. Similar results were obtained at excitation frequencies examined between 80 and 160 kHz.

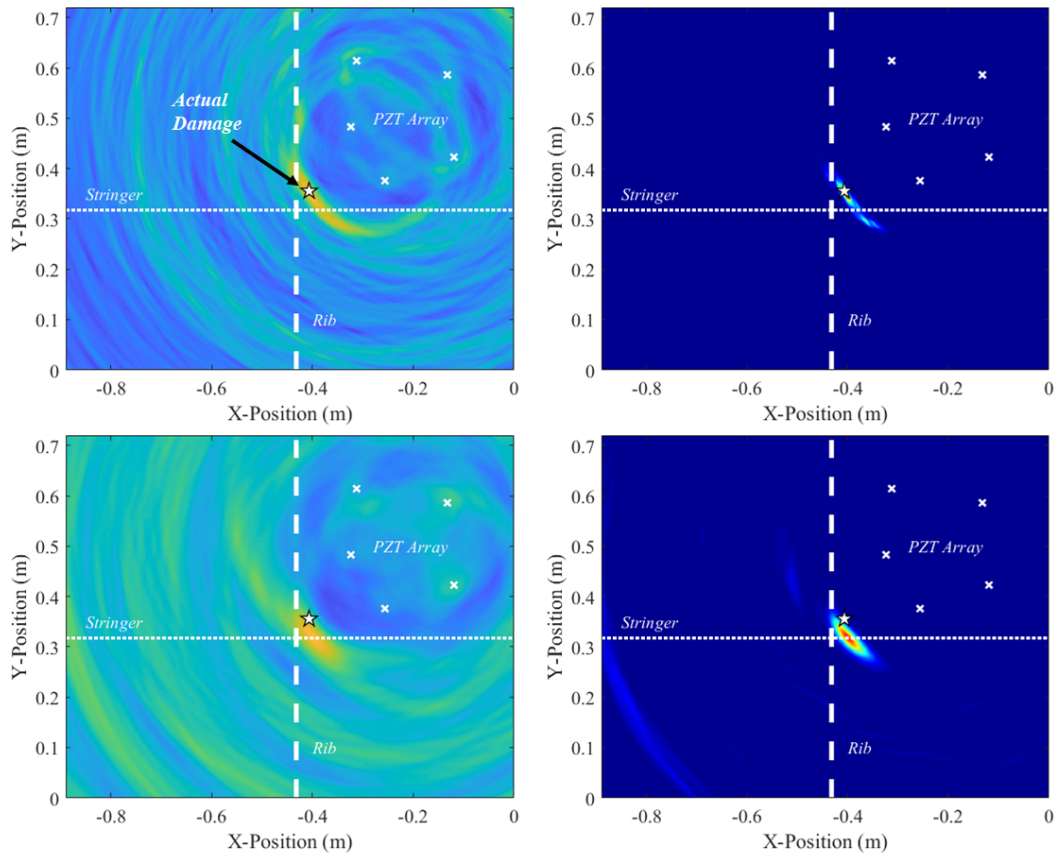


Figure 3.11: Case 1 summation (left) and correlation (right) damage images using the A0 decomposed damage difference signal (top), and S0 decomposed damage difference signals (bottom). The actual damage location is indicated in all images by a star.

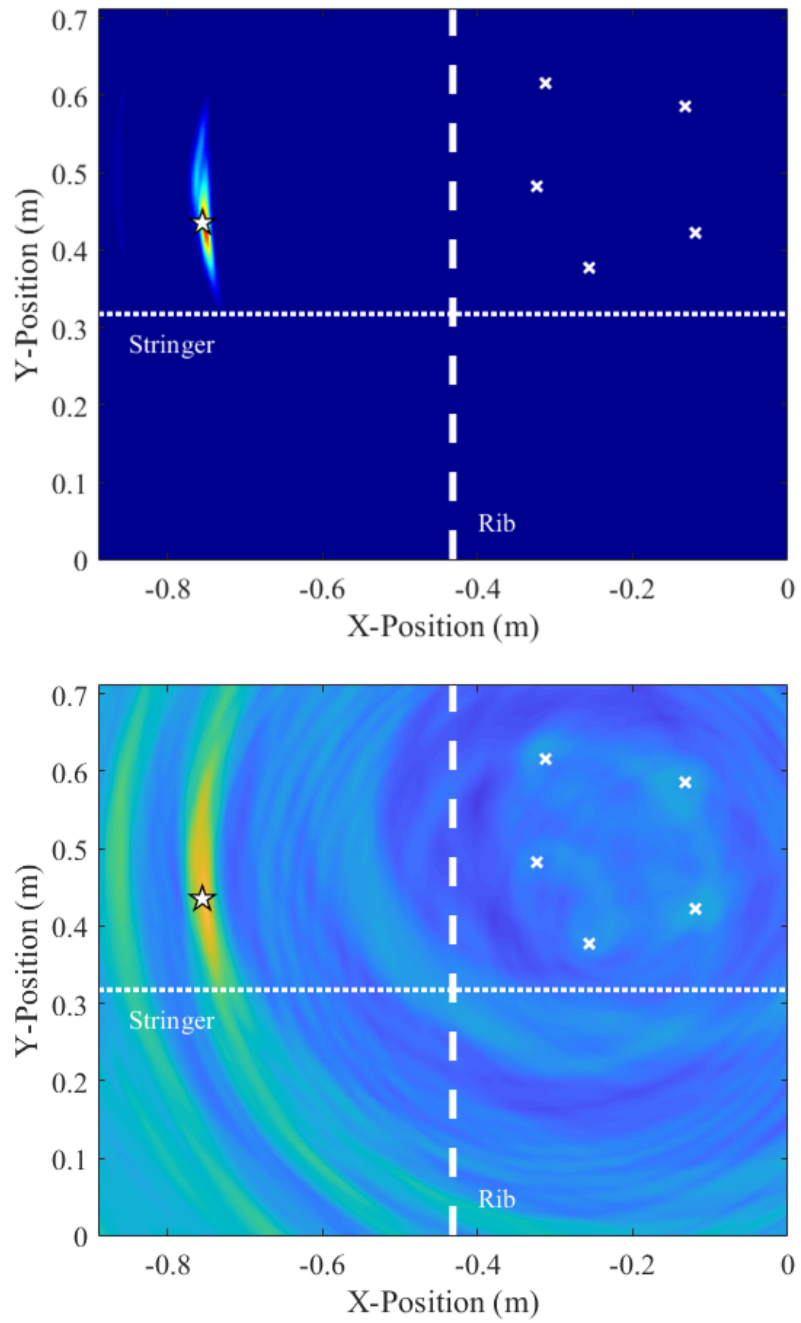


Figure 3.12: Case 2 summation (bottom) and correlation (top) images using the S0 decomposed damage difference signal.

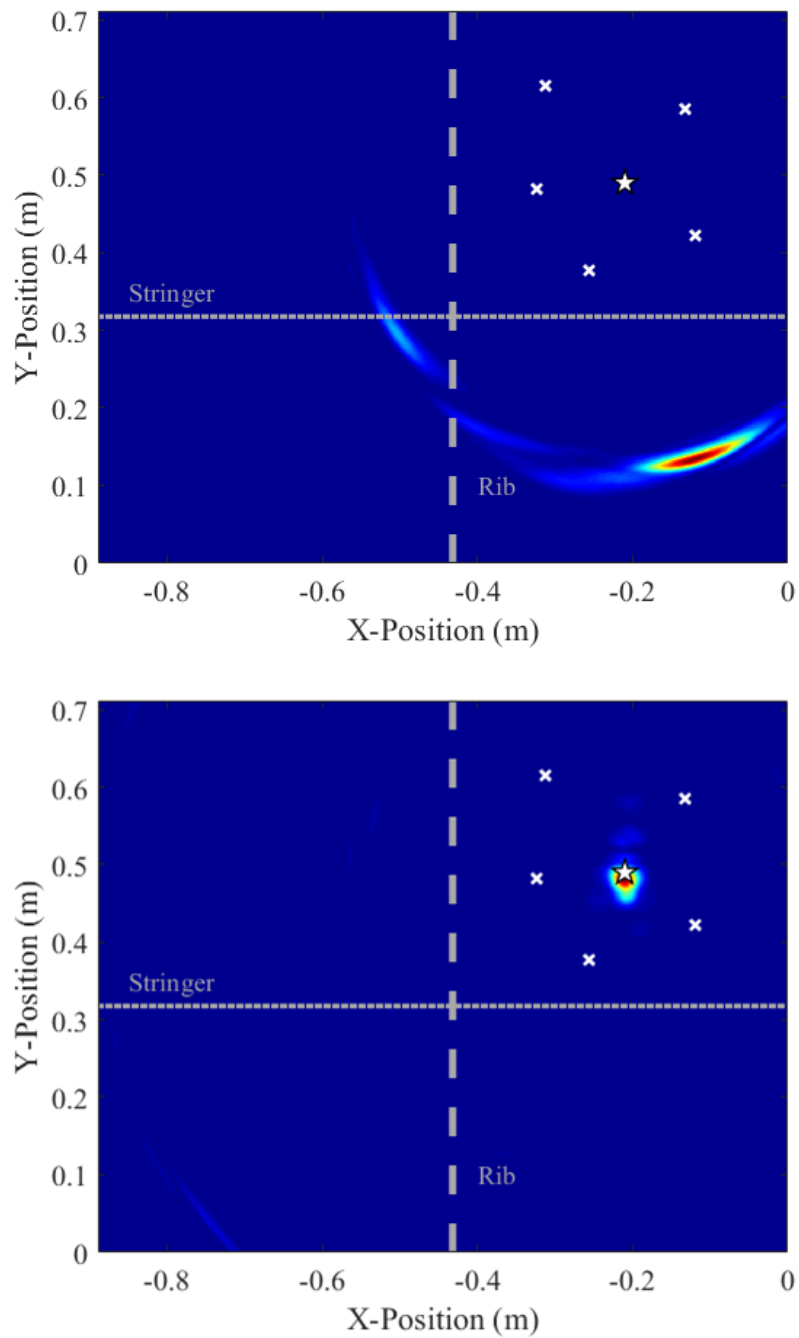


Figure 3.13: Case 3 correlation damage images using the undecomposed damage difference signal (top) and the decomposed S0 damage difference signal (bottom).

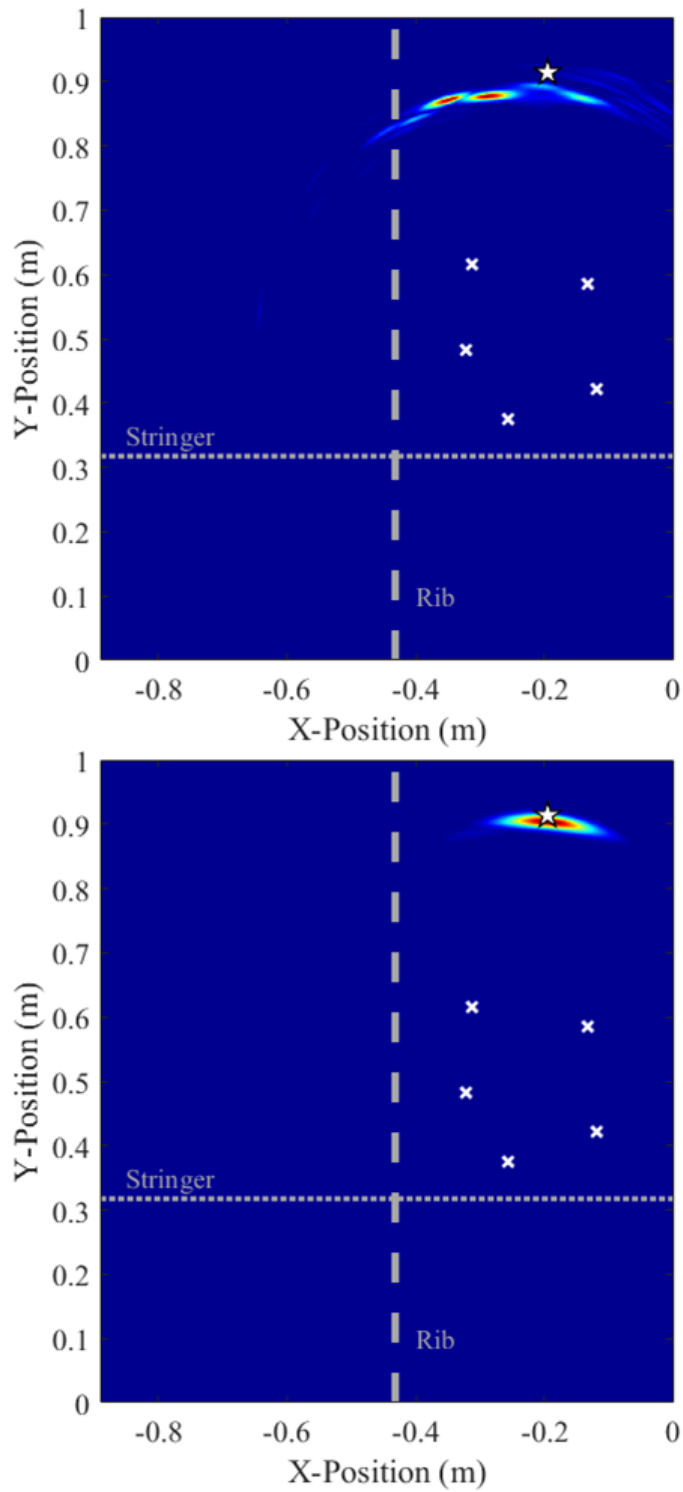


Figure 3.14: Case 4 correlation damage images using the A0 mode decomposed damage difference signal (top) and the S0 mode decomposed damage difference signal (bottom).

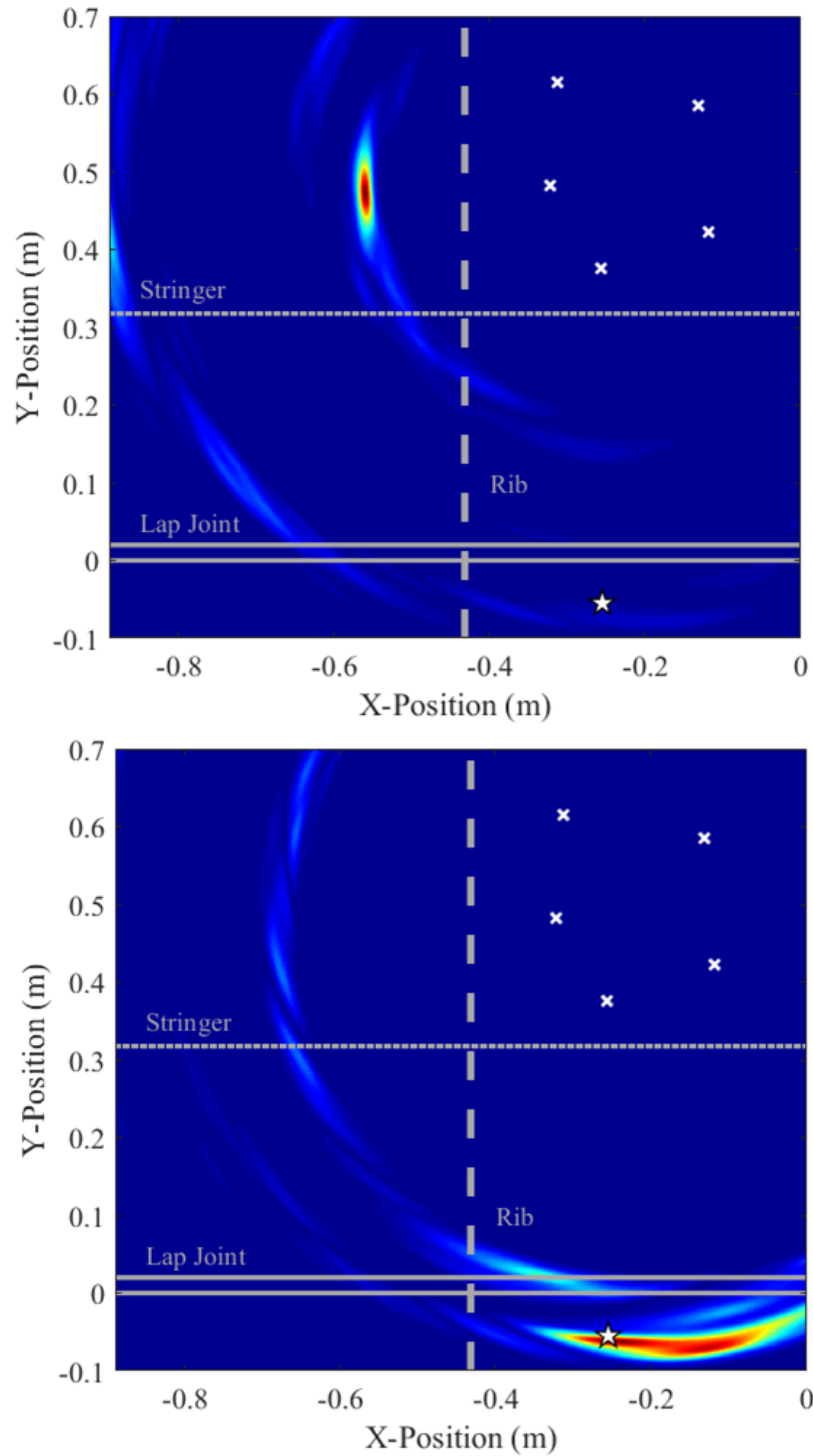


Figure 3.15: Case 5 correlation damage images using the undecomposed damage difference signal (top) and the S0 mode decomposed damage difference signal (bottom).

3.4 Chapter Conclusion

In this chapter, a damage decomposition method using dual element PZT transducers was applied to a sparse array technique based on a guided Lamb Wave damage localization scheme. Experimental studies were performed with an aluminum Piper Cherokee wing since it imposes additional, realistic challenges that are not present when testing with an ideal simple plate. Several cases demonstrated that the sparse array method using dual PZTs to decompose the GLW modes was effective at localizing damage simulated to the wing skin.

It was shown that the S0 mode was more effective in localizing damage in cases farther away from the sensor array (greater than 0.5 m) likely due to the nondispersive nature of the mode. Additionally, the results suggest that the decomposed S0 mode may be used in almost all cases, and this signal is more sensitive to damage at long distances when compared to the undecomposed signal. Use of solely the S0 mode decomposed signal with no required tuning optimization is a significant simplification to the sparse array imaging technique. However, significant effort was needed to determine accurate scaling factors for each transducer pair, and this process could potentially be simplified with more consistent transducer construction and installation.

Finally, the results demonstrate that if a baseline data set is used and measurements are made in a consistent environment, structural features such as stringers, ribs, or lap joints do not significantly influence the damage localization results. The only significant influence is signal attenuation over longer distances and transmission

through multiple structural elements. Lap joints, in particular, would significantly reduce long range damage detection, but the mode decomposition technique improves the detection sensitivity. For the cases shown in this work, no structural features prevented damage from being localized accurately. Thus, these results validate that the presented method can be used to identify and locate crack-like damage in a relatively large section of a wing depending on its construction. This is likely greater than 1 m^2 since actual cracks would yield stronger wave scattering than the magnets used in this work. An array distribution that is optimized over a larger area and not restricted to a featureless section of the plate as presented here may allow for damage detection over an even larger area.

Chapter 4: Conclusion

This thesis presents an investigation into several factors related to industry acceptance of GLW techniques for practical aircraft SHM applications. These factors include the use of GLWs in complex structures, holistic SHM algorithm considerations, human factors in interpretation of data, and improvements to localization sensitivity using nontraditional transducers. These factors and others were studied through two case studies involving actual aircraft structures.

4.1 F/A-18 Wing Torque Loss Monitoring

Chapter 2 investigated the use of a GLW sparse array image compounding technique to detect and localize torque loss in a panel on an F/A-18 wing. A sparse array of PZT transducers was installed on a maintenance access panel and a series of damage studies were performed. Torque loss was introduced to the surrounding panel interface as a means of simulating damage to the structure. The images generated effectively showed accurate locations of loose bolts, and were able to show progressive increase in damage. However, likely due to the complexity of the structure, images were often not as clear as desired or as observed in studies with simplistic metallic plate structures.

Next, various autonomous techniques for determining the location of a loose bolt were investigated. For simple damage cases with a single loose bolt, the techniques presented could effectively locate a loose bolt using the generated TFM images. However, these techniques were essentially limited to this simplistic case of a single loose bolt and would require significant augmentation for more complicated and realistic damage cases. Thus, human interpretation of images was deemed necessary, so a basic blind technician study was conducted to begin to explore human factors involved with such interpretation. Given minimal training, participants were successfully able to find the correct loose bolt within a two bolt radius for multiple trials by examining TFM and compounded spatial damage maps. This confirmed an important fact which is often overlooked or assumed to be true for SHM localization techniques: that a human could accurately interpret the proposed damage maps for at least simple cases. Confirmation of this fact is important for complicated structure applications where images are often not as clean as lab studies with simple plates.

In summary, the results of this study show that examination of SHM techniques from an application perspective exposes the overwhelming complexity involved. Often new GLW SHM techniques are proposed which seem to avoid reference to practical application and focus on overly simplified structures. While basic research in SHM is valuable, growth toward practical application will likely require more systems engineering involvement and development of packaged methods using a combination of existing techniques. Despite the complexity and thickness of the test specimen used in this study, characteristics which are far from ideal for GLW

techniques, the apparent ability to localize fairly small amounts of torque loss was promising.

4.2 Piper Cherokee Wing Damage Localization

Chapter 3 studied the use of nontraditional dual PZT transducers for damage localization in a Piper Cherokee wing. The study first confirmed that Lamb Wave mode decomposition can be achieved using dual PZT transducers, but that significant experimental data was needed to achieve the best decomposition results. This is burdensome for a large sparse array, but it is assumed that the need to determine scaling factors for all transducers could be mitigated through more consistent transducer manufacturing.

Next, five simulated damage cases were introduced to the Piper Cherokee wing and the sparse array damage localization technique was used with dual PZT mode decomposition. Each damage case tested the potential influence of structural features such as ribs, stringers, plate curvature, and lap joints. Simulated damage was clearly located in each case, and complicated structural features did not significantly influence the results. This is because a baseline was used, but for practical purposes, this method can only be used offline (after flight) within a controlled temperature environment. Otherwise, one must explore temperature compensation or a larger set of baseline data. The main observed structural effects were scatter signal attenuation over multiple joints or stiffening features.

Overall, the results demonstrated a very practical application for dual PZT

transducers in a sparse array configuration. Additionally, the results showed that in some damage cases, the use of dual PZTs for mode decomposition improved damage detection sensitivity and accuracy. The mode decomposition technique also reduced restrictions on excitation frequency by eliminating a need to tune excitations to produce a dominant mode. The S0 decomposed signal was able to detect damage in all cases where the A0 mode was dominant. Relying on a single mode is a significant simplification for applying the GLW sparse array technique.

4.3 Future Work

Given lab access to the F/A-18 wing and Piper Cherokee wing specimens, a substantial amount of other damage cases studies could be performed combining GLW techniques and other techniques to form a more holistic SHM approach to a proposed damage scenario. Studies could focus on critical stress hot spots such as the wing-fuselage interface and the main spars throughout the wings. Using the presented access panel torque loss scenario, further human factors evaluations could be performed for complex multi damage location cases. A more rigorous training document may be necessary for this type of study. Additionally, further damage cases using higher, more realistic torque settings should be performed to determine if this has any influence on results.

Significant progress could be made by posing a realistic design challenge for a practical aircraft SHM application. Such a challenge would force exploration of important factors such as system reliability and durability through use of the

aircraft. By posing a real SHM problem with constraints beyond that of a lab setting, new problems applying an SHM system can be discovered and addressed. Additionally, transitioning the lab setup into a more mobile, practical package would add value in increasing technology readiness levels.

Appendix A: Blind Technician Study Details

The following appendix presents the contents of the anonymous technician survey presented in chapter 2. Additionally, the following is a link to a copy of the survey presented to volunteers - https://docs.google.com/forms/d/e/1FAIpQLSeTWd2YFYGK7cUZ122rvctlhxcjfyIAxDGfSRS5vfxkCVCTDw/viewform?usp=sf_link

A.1 Contents of Study Presented to Participants

A.1.1 Instructions

Thank you for volunteering to participate in this study which examines a nondestructive evaluation technique for detecting loose bolts on an aircrafts maintenance access panel (shown in Fig. A.1). You will be presented with seven cases in which a bolt on the panel is looser than the desired torque specification. Your task will be to act as a maintenance inspector by viewing ultrasonic localization images for each case and determining to the best of your ability which bolt is loose. The suggested procedure to follow to interpret these images along with a sample case are presented below.

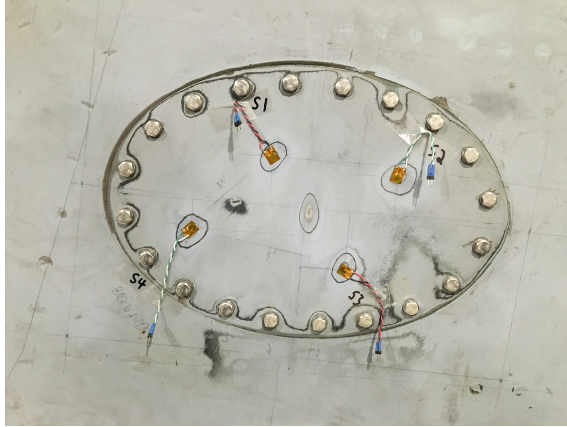


Figure A.1:

A.1.2 Procedure

1. View image (a) and find the location with the darkest red area. It is most likely that the loose bolt is within a 1-3 bolt range of this area, but the highest probability is that it is near the center of the darkest red region.

*** If there are multiple dark red regions, pick the biggest region as the main focus area.

2. View image (b) and look for a patch of yellow to dark red dots near the region identified in step 1. In some cases, there is a larger group of dots near the loose bolt which can be used to confirm the correct bolt.

*** Image (b) may not always provide any useful information. If image (b) shows several large groups of dots or only small scattered dots, ignore this image and rely solely on image (a).

3. Select the loose bolt using the reference numbering schematic and record your response. Please record your response as a number, not a word (ie. 1, 14 etc.).

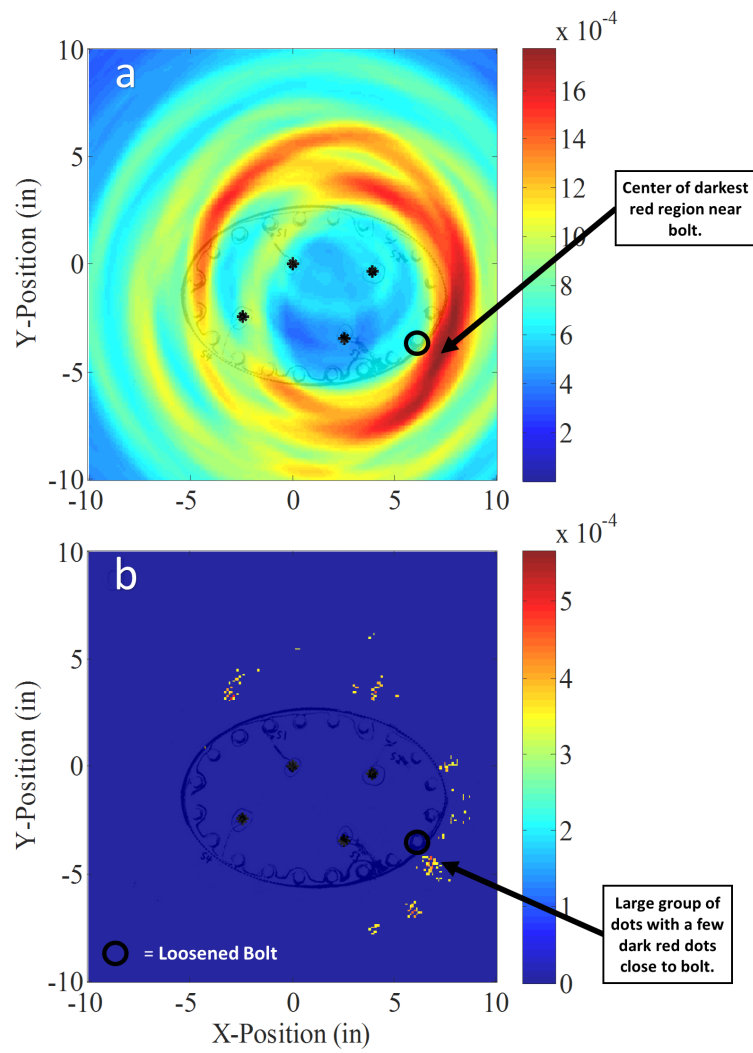


Figure A.2: Example case

In this example case, bolt number 7 was the loosened bolt predominantly indicated by the center of the dark red region of image (a) and confirmed by the large group of dots near the bolt in image (b). Image (a) should always be the primary indicator with image (b) acting as a confirmation only.

Press NEXT to start the survey. You can return to these instructions at any time.

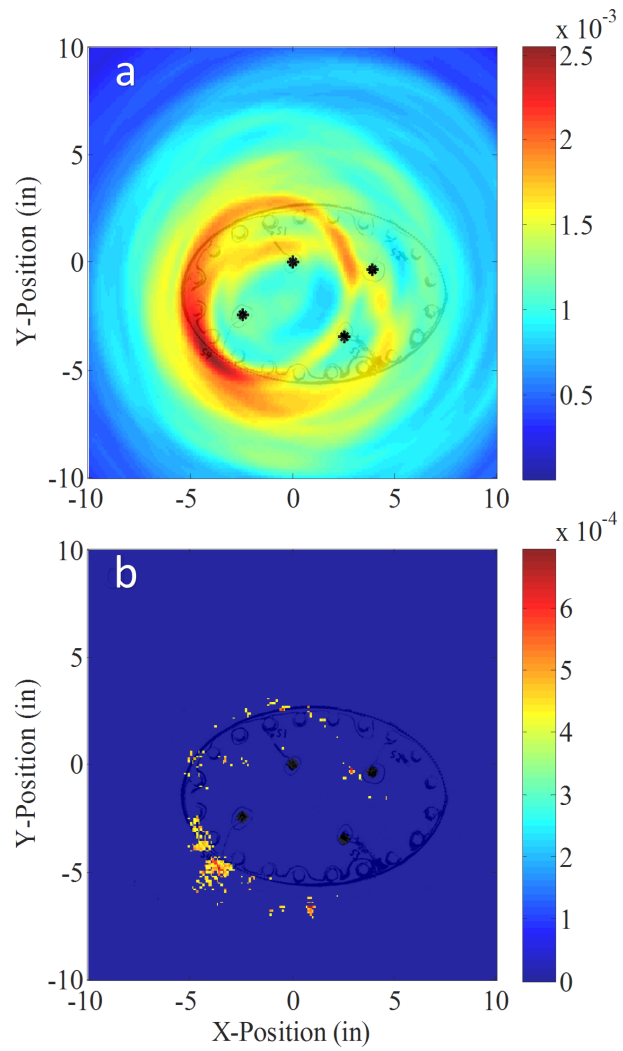


Figure A.3: Case 1 - Which bolt is loose?

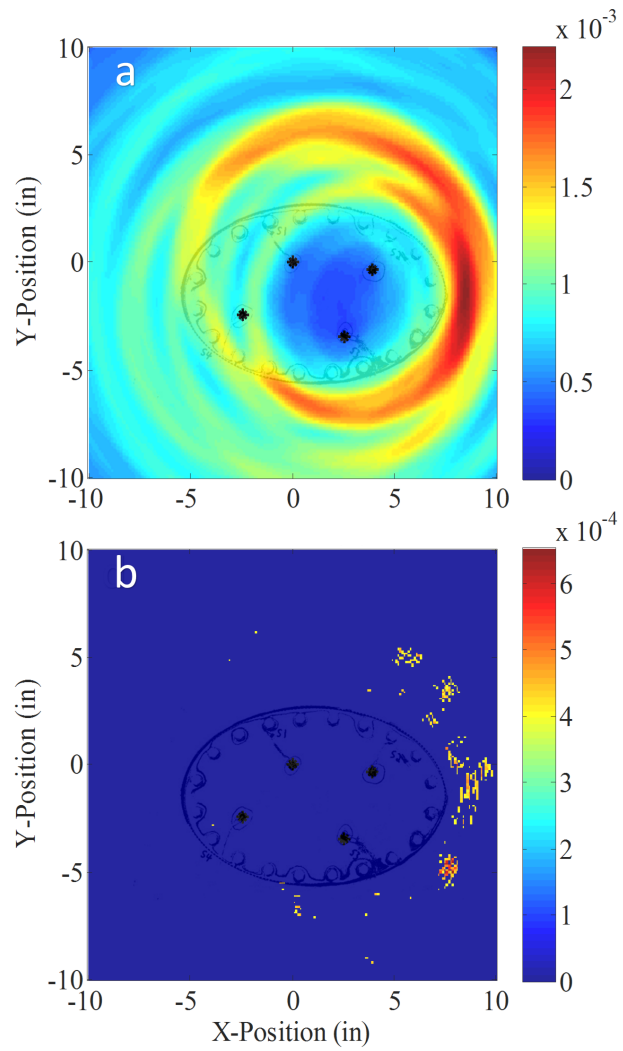


Figure A.4: Case 2 - Which bolt is loose?

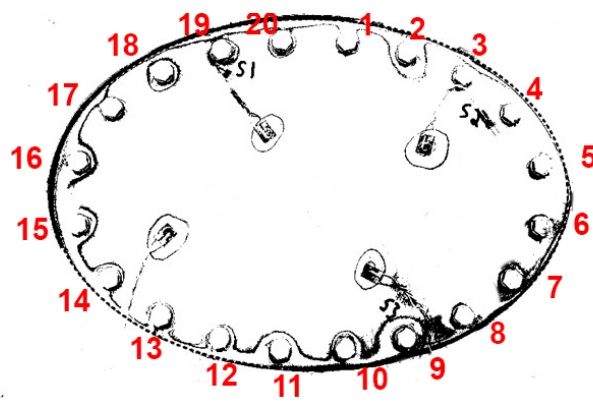
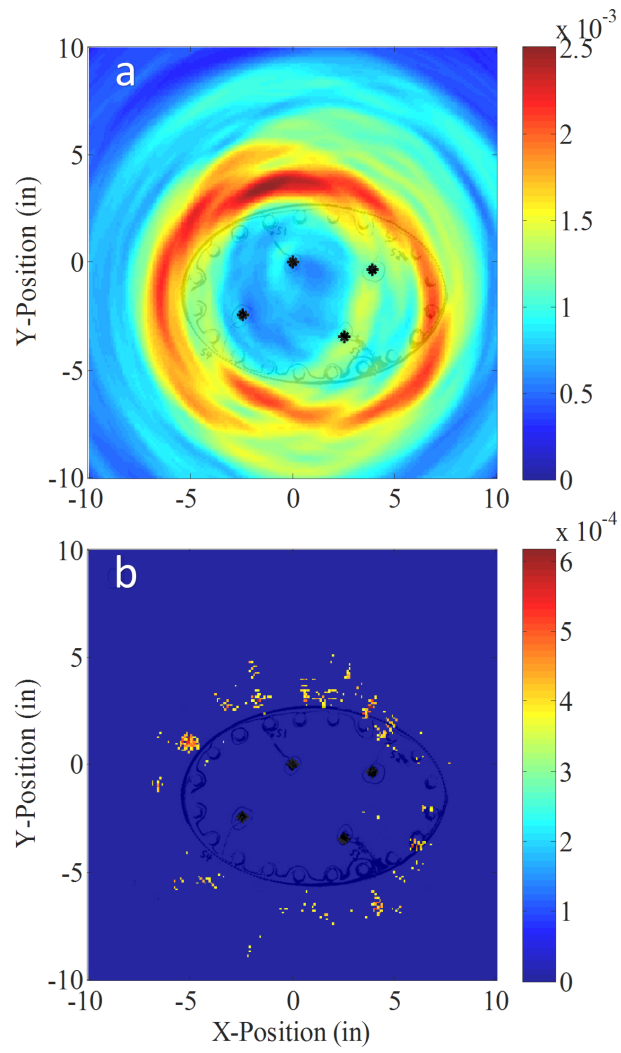


Figure A.5: Case 3 - Which bolt is loose?

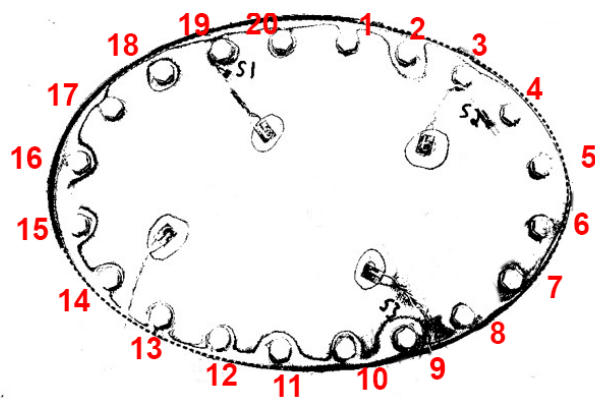
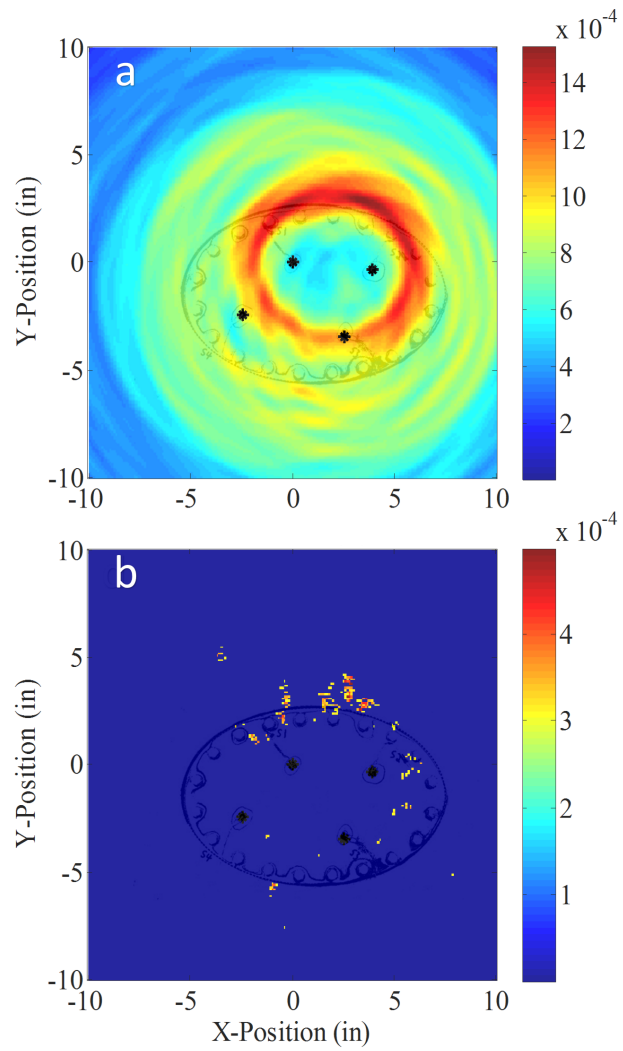


Figure A.6: Case 4 - Which bolt is loose?

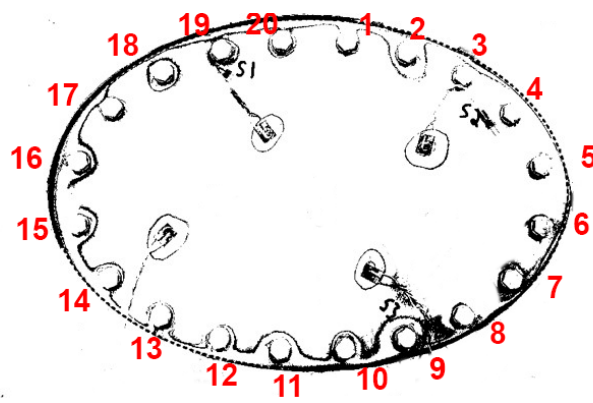
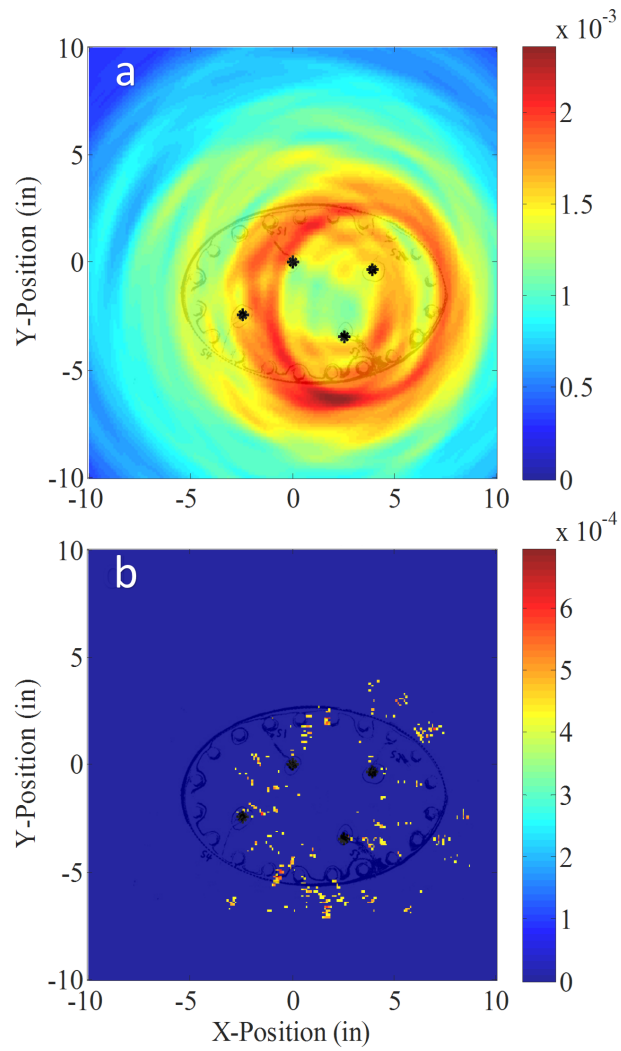


Figure A.7: Case 5 - Which bolt is loose?

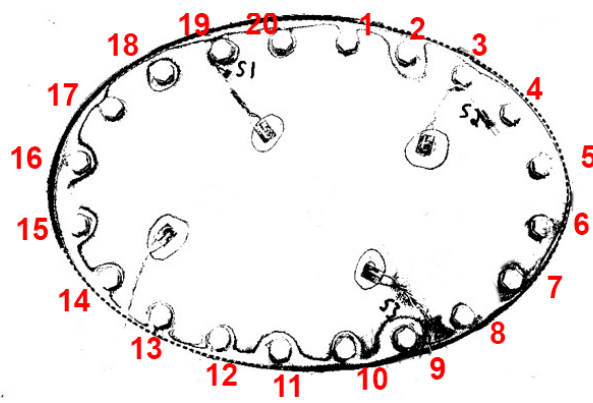
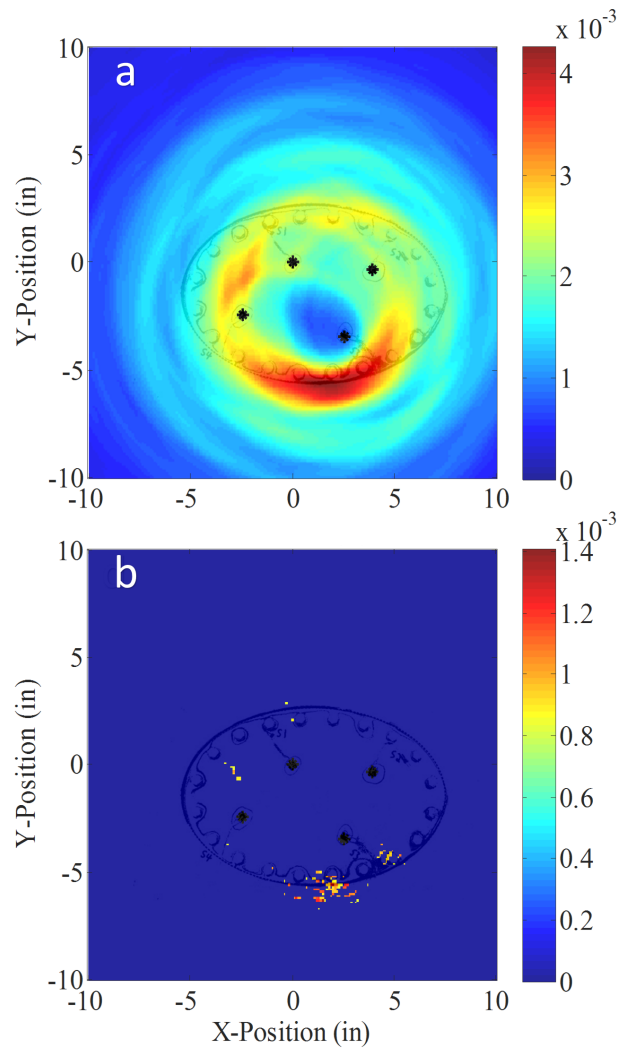


Figure A.8: Case 6 - Which bolt is loose?

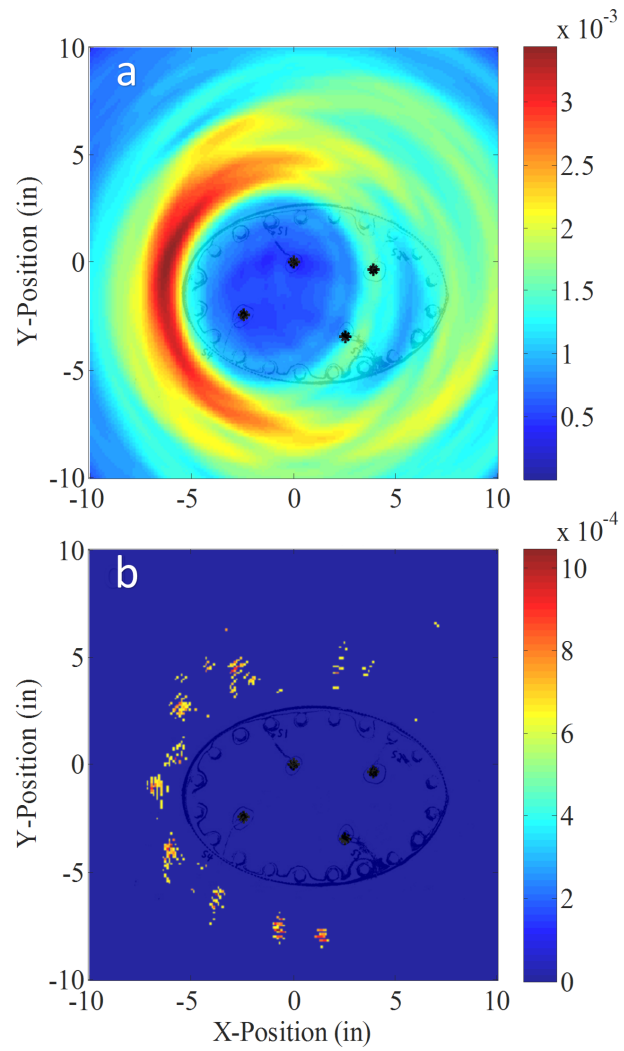


Figure A.9: Case 7 - Which bolt is loose?

Bibliography

- [1] Aviation Statistics. Technical report, NTSB, 2017.
- [2] Jerome Greer Chandler. Industry Challenged By Composite Delamination, September 2012.
- [3] Brendan McGarry. Admiral: Corrosion Damage on F/A-18 Hornets Caught Us by Surprise, June 2015.
- [4] Bjorn Fehrm. Boeings 737 in another pickle, Part 2, October 2019.
- [5] National Transportation Safety Board Aviation Accident Final Report. Technical Report ERA18FA120, NTSB, September 2019.
- [6] National Transportation Safety Board Aviation Accident Final Report. Technical Report DCA11MA039, NTSB, February 2014.
- [7] Scott Maley, John Plets, and Nam D Phan. US Navy Roadmap to Structural Health and Usage Monitoring The Present and Future. In *American Helicopter Society 63rd Annual Forum*, page 12, Virginia Beach, VA, May 2007.
- [8] Anders Rytter. *Vibrational Based Inspection of Civil Engineering Structures*. PhD thesis, Dept. of Building Technology and Structural Engineering, Aalborg University, 1993.
- [9] Victor Giurgiutiu. *Structural Health Monitoring With Piezoelectric Wafer Active Sensors*. Elsevier Inc., 2008.
- [10] Inderjit Chopra and Jayant Sirohi. *Smart Structures Theory*. Cambridge University Press, December 2013.
- [11] Anthony J. Croxford, Paul D. Wilcox, Bruce W. Drinkwater, and George Konstantinidis. Strategies for guided-wave structural health monitoring. *Proceedings of the Royal Society A: Mathematical, Physical and Engineering Sciences*, 463(2087):2961–2981, November 2007.

- [12] Zhongqing Su, Lin Ye, and Ye Lu. Guided Lamb waves for identification of damage in composite structures: A review. *Journal of Sound and Vibration*, 295(3):753–780, August 2006.
- [13] Derek Doyle, Andrei Zagrai, Brandon Arritt, and Hakan akan. Damage Detection in Bolted Space Structures. *Journal of Intelligent Material Systems and Structures*, 21(3):251–264, February 2010.
- [14] Huidong Gao, Y. Shi, and Joseph L. Rose. Guided Wave Tomography on an Aircraft Wing with Leave in Place Sensors. *AIP Conference Proceedings*, 760(1):1788–1794, April 2005.
- [15] Colin Haynes and Michael Todd. Enhanced damage localization for complex structures through statistical modeling and sensor fusion. *Mechanical Systems and Signal Processing*, 54-55:195–209, March 2015.
- [16] Jeong-Beom Ihn and Fu-Kuo Chang. Pitch-catch Active Sensing Methods in Structural Health Monitoring for Aircraft Structures. *Structural Health Monitoring*, 7(1):5–19, March 2008.
- [17] Byungseok Yoo and Ashish Purekar. Corrosion Damage Monitoring Using Guided Lamb Waves. In *ASME 2012 Conference on Smart Materials, Adaptive Structures and Intelligent Systems*, pages 757–764. American Society of Mechanical Engineers Digital Collection, July 2013.
- [18] Ryan P. Dalton, Peter Cawley, and Michael J.S. Lowe. The Potential of Guided Waves for Monitoring Large Areas of Metallic Aircraft Fuselage Structure. *Journal of Nondestructive Evaluation*, 20(1):29–46, March 2001.
- [19] Xinlin Qing, Wenzhuo Li, Yi-Shou Wang, and Hu Sun. Piezoelectric Transducer-Based Structural Health Monitoring for Aircraft Applications. *Sensors*, 19:545, January 2019.
- [20] Jennifer E. Michaels and Thomas E. Michaels. Damage Localization in Inhomogeneous Plates Using a Sparse Array of Ultrasonic Transducers. *AIP Conference Proceedings*, 894(1):846–853, March 2007.
- [21] Holger Speckmann and Jean-Pierre Daniel. Structural Health Monitoring for Airliner, From Research to User Requirements, a European View. In *CANEUS 2004 Conference on Micro-Nano-Technologies*, Monterey, California, November 2004. American Institute of Aeronautics and Astronautics.
- [22] Luis von Ahn, Manuel Blum, and John Langford. Telling Humans and Computers Apart Automatically. *Commun. ACM*, 47(2):56–60, February 2004.
- [23] Guixin Ye, Zhanyong Tang, Dingyi Fang, Zhanxing Zhu, Yansong Feng, Pengfei Xu, Xiaojiang Chen, and Zheng Wang. Yet Another Text Captcha Solver: A Generative Adversarial Network Based Approach. In *Proceedings of the 2018*

- ACM SIGSAC Conference on Computer and Communications Security, CCS '18*, pages 332–348, New York, NY, USA, 2018. ACM. event-place: Toronto, Canada.
- [24] Keith Worden and Graeme Manson. The application of machine learning to structural health monitoring. *Philosophical Transactions of the Royal Society A: Mathematical, Physical and Engineering Sciences*, 365(1851):515–537, February 2007.
- [25] John C. Aldrin, Enrique A. Medina, Daniel A. Allwine, Mohammed Qadeer-Ahmed, Joseph Fisher, Jeremy S. Knopp, and Eric A. Lindgren. Probabilistic Risk Assessment: Impact of Human Factors on Nondestructive Evaluation and Sensor Degradation on Structural Health Monitoring. In *Review of Progress in Quantitative Nondestructive Evaluation*, volume 26, pages 1461–1468, Portland, Oregon (USA), 2007. AIP.
- [26] Catalin Mandache, Marc Genest, Muzibur Khan, and Nezhir Mrad. Considerations on Structural Health Monitoring Reliability. In *NDT in Canada 2011*, page 11, Montreal, CA, November 2011.
- [27] David Mascareas, Crystal Plont, Christina Brown, Martin Cowell, N Jordan Jameson, Jessica Block, Stephanie Djidjev, Heidi Hahn, and Charles Farrar. A vibro-haptic humanmachine interface for structural health monitoring. *Structural Health Monitoring*, 13(6):671–685, November 2014.
- [28] Vander T. Prado, Ricardo T. Higuti, Cludio Kitano, scar Martnez-Graullera, and Julio C. Adamowski. Lamb mode diversity imaging for non-destructive testing of plate-like structures. *NDT & E International*, 59:86–95, October 2013.
- [29] Zenghua Liu, Kunming Sun, Guorong Song, Cunfu He, and Bin Wu. Damage localization in aluminum plate with compact rectangular phased piezoelectric transducer array. *Mechanical Systems and Signal Processing*, 70-71:625–636, March 2016.
- [30] Vanessa Gentzen, Young-Tai Choi, Ashish S. Purekar, and Norman M. Wereley. Experimental Detection and Quantitative Interrogation of Damage in a Jointed Composite Structure. *Journal of Intelligent Material Systems and Structures*, 21(3):275–283, February 2010.
- [31] Zhongqing Su and Lin Ye. Selective generation of Lamb wave modes and their propagation characteristics in defective composite laminates. *Proceedings of the Institution of Mechanical Engineers, Part L: Journal of Materials: Design and Applications*, 218(2):95–110, April 2004.
- [32] Victor Giurgiutiu. Tuned Lamb Wave Excitation and Detection with Piezoelectric Wafer Active Sensors for Structural Health Monitoring. *Journal of Intelligent Material Systems and Structures*, 16(4):291–305, April 2005.

- [33] Hoon Sohn and Sang Jun Lee. Lamb wave tuning curve calibration for surface-bonded piezoelectric transducers. *Smart Materials and Structures*, 19(1):015007, November 2009.
- [34] Hoon Sohn and Seuno Bum Kim. Development of dual PZT transducers for reference-free crack detection in thin plate structures. *IEEE Transactions on Ultrasonics, Ferroelectrics, and Frequency Control*, 57(1):229–240, January 2010.
- [35] Chul Min Yeum, Hoon Sohn, and Jeong Beom Ihn. Lamb wave mode decomposition using concentric ring and circular piezoelectric transducers. *Wave Motion*, 48(4):358–370, June 2011.
- [36] Jennifer E. Michaels and Thomas E. Michaels. Enhanced Differential Methods for Guided Wave Phased Array Imaging Using Spatially Distributed Piezoelectric Transducers. *AIP Conference Proceedings*, 820(1):837–844, March 2006.
- [37] Nazih Mechbal, Marc Rebillat, and Mikhail Guskov. A Probabilistic Approach to Structural Health Monitoring of Composite Aircraft Nacelles: Implementation and Validation. In *21st International Conference on Composite Materials*, Xi'an, China, August 2017.
- [38] Wang Qiang and Yuan Shenfang. Baseline-free Imaging Method based on New PZT Sensor Arrangements. *Journal of Intelligent Material Systems and Structures*, 20(14):1663–1673, May 2009.
- [39] Hoon Sohn, Hyun Woo Park, Kincho H. Law, and Charles R. Farrar. Combination of a Time Reversal Process and a Consecutiv Outlier Analysis for Baseline-free Damage Diagnosis. *Journal of Intelligent Material Systems and Structures*, 18(4):335–346, April 2007.
- [40] George Konstantinidis, Bruce W. Drinkwater, and Paul D. Wilcox. The temperature stability of guided wave structural health monitoring systems. *Smart Materials and Structures*, 15(4):967–976, June 2006.
- [41] Olivier Diligent, Tomas Grahn, Anders Bostrm, Peter Cawley, and Michael J.S. Lowe. The low-frequency reflection and scattering of the S0 Lamb mode from a circular through-thickness hole in a plate: Finite Element, analytical and experimental studies. *The Journal of the Acoustical Society of America*, 112(6):2589–2601, December 2002.
- [42] Mark K. Hinders. Lamb Wave Scattering from Rivets. In Donald O. Thompson and Dale E. Chimenti, editors, *Review of Progress in Quantitative Nondestructive Evaluation: Volume 15A*, pages 209–216. Springer US, Boston, MA, 1996.
- [43] Zensheu Chang and Ajit Mal. Scattering of Lamb waves from a rivet hole with edge cracks. *Mechanics of Materials*, 31(3):197–204, March 1999.

- [44] Chul Min Yeum, Hoon Sohn, Hyung Jin Lim, and Jeong Beom Ihn. Reference-free delamination detection using Lamb waves. *Structural Control and Health Monitoring*, 21(5):675–684, 2014.
- [45] Lingyu Yu, Giola Bottai-Santoni, and Victor Giurgiutiu. Shear lag solution for tuning ultrasonic piezoelectric wafer active sensors with applications to Lamb wave array imaging. *International Journal of Engineering Science*, 48(10):848–861, October 2010.